

Phase-field modelling of mechanical wave propagation in polycrystalline materials: Validation study

Xiaoying Liu ^{a,b,*}, Daniel Schneider ^{b,c}, Britta Nestler ^{b,c}

^a School of Materials Science and Engineering, Shandong University, Jinan, 250061, PR China

^b Institute for Applied Materials (IAM-MMS), Karlsruhe Institute of Technology, Karlsruhe, 76131, Germany

^c Institute of Digital Materials Science (IDM), Karlsruhe University of Applied Sciences, Karlsruhe, 76133, Germany

ARTICLE INFO

Keywords:

Multiphase field

Homogenization scheme

Mechanical wave

Dynamic mechanical analysis

ABSTRACT

With all the great advances in phase-field modelling combined with continuum mechanics, a detailed accuracy and convergence analysis about the influence of the diffuse interface upon the dynamic mechanical energy is still missing. Based on the previous work, i.e. deriving the homogenization scheme on the basis of balance conditions and embedding the high-order discontinuous Galerkin method into the phase field method, the influence of the diffuse interface, especially the multiphase/multigrain interface, on the dynamic mechanical energy is studied by considering the factors, such as the wave types, the material properties, the phase/grain size, the interface width and the normal vector formula. The numerical results are compared with the sharp-interface results to show the accuracy and stability, and with the linear homogenization method to demonstrate the advantages of the proposed scheme. The research work in this paper will build the foundation for the future simulation of rapid solid phase transformation.

1. Introduction

A large number of natural and manufactured solids are polycrystalline, e.g. ice, metals, alloys, ceramics, composites, rocks and so on. The polycrystalline materials are composed of numbers of mesoscopic phases/grains, which are physically separated by boundaries, i.e. interfaces. In general, phases/grains in polycrystalline materials can consist of different components, orientations and different geometrical shapes and sizes, which in its entirety influences the macroscopic material properties. Moreover, the nucleation and growth of phases/grains are driven by various factors, such as the entropy density, the chemical potential, the mechanical energy and others. This means that the macroscopic properties of polycrystalline material are significantly influenced by the aforementioned factors, through the process of microstructural evolution. Therefore, it is desirable to develop numerical methods that are able to comprehensively investigate the individual microstructural quantities within a multiscale modelling framework, i.e. the mesoscopic microstructural evolution and the macroscopic material properties.

In order to study the process of microstructural evolution and its influence on the macroscopic material properties, phase field modelling has been rapidly developed into a robust numerical tool over the last decades, based on the fundamental work of Ginzburg and Landau (1950), Cahn and Hilliard (1958) and Allen and Cahn (1972). By diffusing the sharp interface with order parameters, the phase field

method saves the large amount of effort required to trace the interface. By introducing a vector valued order parameter ϕ , with multiple components ϕ_α representing different phases/grains, the free energy density varies smoothly across the interface. As a result, the sharp interface of infinitesimal thickness is approximated by a diffuse interface of finite thickness. Therefore, the free boundary problem is addressed by solving the evolution equations of the order parameters, deriving the driving force according to the bulk energy within the phases/grains (Moelans et al., 2008; Wang and Li, 2010; Jacqmin, 1999). Meanwhile, the motion of the interface is implicitly expressed through the evolution of order parameters. During the evolution process of the order parameters, the conservation laws for physical fields such as energy, momentum and mass are observed. The phase field method has been combined with various physical fields and has been successfully applied in the simulation of various microstructural evolution processes, such as solidification (Nestler et al., 2005; Nestler and Wheeler, 2002; Karma and Rappel, 1998; Folch and Plapp, 2005), precipitation and dissolution (Chen et al., 2004; Xu and Meakin, 2008), austenitic decomposition (Miltzer, 2011; Yeddu et al., 2012), martensitic transformation (Xi and Su, 2021; Mamivand et al., 2013; Artemev et al., 2000), electric polarization (Zhang and Su, 2022), as well as crack initiation and propagation (Ambati et al., 2015; Spatschek et al., 2006; Wilson and Landis, 2016; Henry, 2019).

* Corresponding author at: Institute for Applied Materials (IAM-MMS), Karlsruhe Institute of Technology, Karlsruhe, 76131, Germany.
E-mail address: xiaoying.liu@kit.edu (X. Liu).

Table 1
Nomenclature.

$a(\phi, \nabla\phi)$	Gradient energy density	$\overline{\mathcal{M}}$	Local effective density matrix
$a_{ij}(t)$	Time decomposition of $u_i(x, t)$	$\mathbf{M}_\sigma/\mathbf{M}_\varepsilon$	Transformation matrix
$b_{ij}(t)$	Time decomposition of $s_i(x, t)$	$M_{\alpha\beta}$	Mobility for $\alpha - \beta$ interface
\mathbf{C}^k	Coefficient matrix	$p_j(\mathbf{x})$	Space decomposition of u_i/s_i
\mathbf{D}^k	Matrix calculated by \mathbf{G}^k and \mathbf{H}^k	\mathbf{Q}	Transformation matrix
E^t	Transmitted energy	R_K	Stiffness ratio
E^r	Reflected energy	R_p	Density ratio
\mathcal{F}	Free energy	R_e	Transmission ratio
$f_d(\phi, \varepsilon, v)$	Dynamic mechanical energy density	$s_i(x, t)$	Source term to $u_i(x, t)$
$f_e(\phi, \varepsilon)$	Elastic strain energy density	T^{S_c}	Transformation matrix
$f_k(\phi, v)$	Kinetic energy density	t	Time
$f_L^a(\tilde{\sigma}_n, \tilde{\varepsilon}_i)$	Legendre transform of $f_\varepsilon^a(\varepsilon^a)$	\mathbf{u}	Stress and velocity vector
$f_i(x, t)$	Mechanical wave source	\mathbf{v}	Material particle velocity
\mathbf{G}^k	Matrix for the eigenvectors of \mathbf{C}^k	$\tilde{\mathbf{v}}$	Local material particle velocity
\mathbf{H}^k	Matrix for the eigenvalues of \mathbf{C}^k	$w_i(x, t)$	Displacement
$h_n(\phi)$	Interpolation function	\mathbf{x}	Global Cartesian coordinate
\mathbf{K}	Effective stiffness matrix	$\gamma_{\alpha\beta}$	Surface energy
$\overline{\mathbf{K}}$	Stiffness matrix	ε	Elastic strain tensor
$\tilde{\mathbf{K}}$	Local stiffness matrix	$\tilde{\varepsilon}$	Local elastic strain tensor
$\hat{\mathbf{K}}$	Stiffness matrix in $f_L(\tilde{\sigma}_n, \tilde{\varepsilon}_i)$	e	Interface width parameter
$\tilde{\mathbf{K}}$	Local effective stiffness matrix	$\{\xi, \eta, \zeta\}$	Local base unit vectors
L	Interface width	σ	Stress tensor
\mathcal{M}	Effective density matrix	$\tilde{\sigma}$	Local stress tensor
$\overline{\mathcal{M}}$	Density matrix	ϕ	N -tuples order parameters
$\tilde{\mathcal{M}}$	Local density matrix	$\omega(\phi)$	Potential energy density

To solve the evolution equations of order parameters, where the variational derivative of the density of free energy with respect to order parameters and their gradients acts as the driving force, the homogenization approach is most commonly used in the phase field community. To obtain a correct profile at the diffuse interface, the homogenization methods should ensure that the energy density at the diffuse interface varies smoothly and obeys the conservation law (Schneider et al., 2018; Durga et al., 2013).

For the homogenization of mechanical energy density, the Voigt/Taylor (VT) model (Voigt, 1889) assumes that the strain values are constants across the diffuse interface. The Reuss/Sachs (RS) model (Reuß, 1929) was established based on the assumption that the stress values are invariable across the diffuse interface. By making an analogy between the elastic stress and the generalized chemical potential, the postulate and formula in Steinbach and Apel (2006) resemble the RS model. The Khachaturyan model (Khachaturian, 1983) adopted the VT model as the homogenization scheme for the stiffness matrix, while the RS model adopted the model for the eigenstrain. Ammar et al. (2009) have made a detailed comparison between these models, in terms of establishment, derivation and application. Mosler et al. (2014) proposed a new homogenization approach based on the incremental energy minimization, where the energy profile is bounded by the VT and the RS models. Kiefer et al. (2017) compared the convergence rate of different homogenization models, including VT, RS and rank one convexification approaches, using numerical examples. By analysing the interfacial excess contribution to the energy, Durga et al. (2013) applied the VT model in the direction parallel to the interface, while applied the Steinbach/Apel model (Steinbach and Apel, 2006) in the direction normal to the interface. Based on the similar assumptions for stress and strain components, Schneider et al. (2015) proposed a sophisticated homogenization model according to the force balance and Hadamard jump conditions, which is free from the problem of interfacial excess energy (Schneider et al., 2018). This homogenization scheme has been successfully applied in elastic deformation (Schneider et al., 2015), elasto plastic modelling (Herrmann et al., 2018), finite deformation (Schneider et al., 2017) and Chemo elastic simulation (Amos et al., 2018). Similarly, Liu et al. (2021) derived the homogenization scheme for the mechanical wave on the basis of the equilibrium conditions at the sharp interface, and the high order discontinuous Galerkin method (Hu et al., 1999; Wilcox et al., 2010; Käser and Dumbser, 2006; Kronbichler et al., 2016) was embedded into the phase field method to improve the numerical accuracy.

Fantoni et al. (2020), Fantoni and Bacigalupo (2020) used the asymptotic homogenization scheme to respectively study the damage propagation and wave propagation in periodic microstructured materials. By coupling the finite element method with the modelling of the multiphase field, Nakahata et al. (2016) implemented the ultrasonic simulation for the non destructive testing of polycrystalline structures. Li et al. (2019) investigated the dynamic interaction between the defects and the longitudinal sound wave with the phase field model. However, a detailed accuracy and convergence study about the influence of the homogenization scheme upon the dynamic mechanical energy has been rarely studied and reported so far, especially the homogenization scheme at the multiphase/multigrain interface. Therefore, based on the previous work by Liu et al. (2021), a detailed parameter study of the dynamic mechanical energy will be carried out in this paper.

The remaining part of this paper is organized as follows. Based on the phase field method, the parametrization of phases/grains in the multiphase/multigrain system will be introduced in Section 2. The homogenization scheme for mechanical wave is briefly reviewed in Section 3. Section 4 provides the methods for deriving the vector normal to the diffuse interface in a multiphase/multigrain system, which is ambiguous but essential to the homogenization scheme in Section 3. The definitions for mechanical wave with a strong and weak discontinuity are introduced in Section 5, and the governing equations for mechanical wave propagation, as well as the high order numerical approximation with the Riemann solver, are presented in Section 6. With the benchmark examples, Section 7 analyses the dynamic mechanical energy, considering the aspects of the wave types, the material properties, the phase/grain size, the interface width and the normal vector formula, through which numerical accuracy and stability are maintained. The numerical results are also compared with those from the linear homogenization method, i.e. the VT model, to demonstrate the advantages of the proposed scheme. The conclusions are given in Section 8.

2. Parametrization

For the symbols and equations in this paper, the following conventions apply: (1) the scalar variables are written as regular upper case/lowercase letters, (2) the bold lowercase letters represent vectors, (3) the bold uppercase letters denote matrices and (4) for the lowercase Latin subscripts/superscripts in the equations, the index notation and

the Einstein summation convention apply, if no further instructions are given. The nomenclature is provided in [Table 1](#).

In a multiphase/multigrain model with N phases/grains, the total free energy F is calculated as ([Nestler et al., 2005](#); [Schneider et al., 2018](#)):

$$F = \int_V \left(\epsilon a(\boldsymbol{\phi}, \nabla \boldsymbol{\phi}) + \frac{1}{\epsilon} \omega(\boldsymbol{\phi}) + f_d(\boldsymbol{\phi}, \boldsymbol{\epsilon}, \boldsymbol{\nu}) + f(\dots) \right) dV. \quad (1)$$

With ϕ_α defined as the volume fraction of ordering state (phase/grain) α and ∇ as the gradient operator, the N tuples read $\boldsymbol{\phi} = (\phi_1, \phi_2, \dots, \phi_N)$ and $\nabla \boldsymbol{\phi} = (\nabla \phi_1, \nabla \phi_2, \dots, \nabla \phi_N)$. Supposing that $\gamma_{\alpha\beta}$ denotes the surface energy of the interface between two neighbouring phases/grains α and β , the gradient energy density $a(\boldsymbol{\phi}, \nabla \boldsymbol{\phi})$ is expressed as:

$$a(\boldsymbol{\phi}, \nabla \boldsymbol{\phi}) = \sum_{\alpha, \beta > \alpha}^N \gamma_{\alpha\beta} \left| \phi_\alpha \nabla \phi_\beta - \phi_\beta \nabla \phi_\alpha \right|^2, \quad (2)$$

where $|\cdot|$ provides the length of a vector or the absolute value of a scalar. The potential energy density $\omega(\boldsymbol{\phi})$ can take the form of either obstacle or well type ([Nestler et al., 2005](#)):

$$\omega_{ob}(\boldsymbol{\phi}) = \frac{16}{\pi^2} \sum_{\alpha, \beta > \alpha}^N \gamma_{\alpha\beta} \phi_\alpha \phi_\beta + \sum_{\alpha, \beta > \alpha, \delta > \beta}^N \gamma_{\alpha\beta\delta} \phi_\alpha \phi_\beta \phi_\delta, \quad (3a)$$

$$\omega_{we}(\boldsymbol{\phi}) = 9 \sum_{\alpha, \beta > \alpha}^N \gamma_{\alpha\beta} \phi_\alpha^2 \phi_\beta^2 + \sum_{\alpha, \beta > \alpha, \delta > \beta}^N \gamma_{\alpha\beta\delta} \phi_\alpha^2 \phi_\beta^2 \phi_\delta^2. \quad (3b)$$

The second term on the right hand side of Eq. (3) can efficiently prevent the appearance of the artificial third phase in the two phase region. With $\boldsymbol{\epsilon}$ and $\boldsymbol{\nu}$ respectively representing the infinitesimal elastic strain tensor in the Voigt notation and the material particle velocity vector, $f_d(\boldsymbol{\phi}, \boldsymbol{\epsilon}, \boldsymbol{\nu})$ denotes the dynamic mechanical energy density. $f(\dots)$ in Eq. (1) represents the additional energy density contributed by other physical fields.

The order parameter $\phi_\alpha(\mathbf{x}, t)$ ($\alpha = 1, 2, \dots, N$) physically represents the volume fraction of the phase/grain α at location $\mathbf{x} = \{x_1, x_2, x_3\}$ and time t , which therefore satisfies the following constraint:

$$\sum_{\alpha}^N \phi_\alpha(\mathbf{x}, t) = 1, \quad 0 \leq \phi_\alpha(\mathbf{x}, t) \leq 1. \quad (4)$$

Thereby, the multiphase/multigrain model is parametrized by order parameter ϕ_α , and [Fig. 1](#) is illustrated as an exemplification. Specifically, $\phi_\alpha = 1$ within the regions containing a single phase/grain α , while $\phi_\alpha = 0$ in the domains comprised of a single phase/grain β ($\beta \neq \alpha$). Between the single phase/grain regions, there are finite thickness interfaces, across which the order parameters vary continuously and smoothly and satisfy Eq. (4) in the meantime, as illustrated on the right side in [Fig. 1](#).

The parameter ϵ in Eq. (1) is related to the width of diffuse interface. According to the study by [Selzer et al. \(2010\)](#), the interface thickness is in direct proportion to the parameter ϵ for the pure substances. But in the binary system, the phase diagram plays an important role in determining the interface thickness. When the difference of concentrations between different phases increases, the influence of parameter ϵ on the interface width decreases.

In this paper, the entire simulation was implemented with the multifunctional numerical analysis software PACE3D¹ ([Hötzer et al., 2018](#)), where the whole simulated domain is discretized into numbers of cubic cells, by an equidistant grid. In the equilibrium state in PACE3D, the relationship between the interface width L and the parameter ϵ can be estimated as:

$$L \approx 2.5 \cdot \epsilon \cdot \Delta x_1, \quad (5)$$

where $\Delta x_1 = \Delta x_2 = \Delta x_3$ is the side length of each cell.

¹ PACE3D (Parallel Algorithms for Crystal Evolution in 3D) is developed by the research group of Prof. Dr. rer. nat. Britta Nestler, at the Karlsruhe Institute of Technology and the Karlsruhe University of Applied Sciences.

From the viewpoint of the sharp interface approximation, the interface thickness should be ‘‘sufficiently small’’ to approximate the sharp interface model with the phase field solution. However, from the viewpoint of numerical stability and applicability, the numerical results should not depend, or decrease their dependence, on the interface thickness. In our previous work ([Liu et al., 2021](#)), the influence of the interface width is studied from the aspect of the ratio between the minimum wavelength and the maximum interface width, in a 1D case with two different phases. In this paper, the influence of the interface thickness on the numerical results is analysed in Section 7.3, through a 2D example with a multiphase/multigrain interface.

By parametrizing the whole domain with order parameters, the formula for the dynamic mechanical energy density $f_d(\boldsymbol{\phi}, \boldsymbol{\epsilon}, \boldsymbol{\nu})$ in Eq. (1) is expressed as:

$$f_d(\boldsymbol{\phi}, \boldsymbol{\epsilon}, \boldsymbol{\nu}) = \sum_{\alpha}^N f_d^{\alpha}(\boldsymbol{\epsilon}^{\alpha}, \boldsymbol{\nu}^{\alpha}) h_{\alpha}(\boldsymbol{\phi}), \quad (6)$$

where $f_d^{\alpha}(\boldsymbol{\epsilon}^{\alpha}, \boldsymbol{\nu}^{\alpha})$ is the dynamic mechanical energy density for the phase/grain α , and the interpolation function $h_{\alpha}(\boldsymbol{\phi})$ is calculated as:

$$h_{\alpha}(\boldsymbol{\phi}) = \frac{\bar{h}_{\alpha}(\phi_{\alpha})}{\sum_{\beta}^N \bar{h}_{\beta}(\phi_{\beta})}. \quad (7)$$

Here, the function $\bar{h}_{\alpha}(\phi_{\alpha})$ can take one of the following three different formats:

$$\bar{h}_{\alpha}(\phi_{\alpha}) = \begin{cases} \phi_{\alpha} \\ \phi_{\alpha}^2 (3 - 2\phi_{\alpha}) \\ \phi_{\alpha}^3 (6\phi_{\alpha}^2 - 15\phi_{\alpha} + 10) \end{cases} \quad (8)$$

From Eqs. (7) and (8), it is observed that the interpolation function $h_{\alpha}(\boldsymbol{\phi})$ satisfies $\sum_{\alpha}^N h_{\alpha}(\boldsymbol{\phi}) = 1$ ($0 \leq h_{\alpha}(\boldsymbol{\phi}) \leq 1$), similar to the order parameter ϕ_{α} .

With the volume fraction $\boldsymbol{\phi}$, the free boundary problem during the process of microstructural evolution is therefore solved by simulating the evolution of order parameters [Steinbach and Pezzolla \(1999\)](#):

$$\dot{\phi}_{\alpha}(\mathbf{x}, t) = -\frac{1}{N} \sum_{\beta(\beta \neq \alpha)}^N M_{\alpha\beta} \left(\frac{\delta F}{\delta \phi_{\alpha}} - \frac{\delta F}{\delta \phi_{\beta}} \right), \quad (9)$$

where $\dot{\phi}_{\alpha} = \partial \phi_{\alpha} / \partial t$ represents the first order partial derivative of the order parameter ϕ_{α} , with respect to time t . $M_{\alpha\beta}$ is the individual mobility for each $\alpha - \beta$ interface. With $\nabla \cdot$ as the divergence operator, the variation of the total energy $\delta F / \delta \phi_{\alpha}$ is expressed as:

$$\frac{\delta F}{\delta \phi_{\alpha}} = \left(\frac{\partial}{\partial \phi_{\alpha}} - \nabla \cdot \frac{\partial}{\partial \nabla \phi_{\alpha}} \right) \left(\epsilon a(\boldsymbol{\phi}, \nabla \boldsymbol{\phi}) + \frac{1}{\epsilon} \omega(\boldsymbol{\phi}) + f_d(\boldsymbol{\phi}, \boldsymbol{\epsilon}, \boldsymbol{\nu}) + f(\dots) \right). \quad (10)$$

3. Homogenization scheme for mechanical wave

During the process of mechanical wave propagation, the corresponding energy density $f_d(\boldsymbol{\phi}, \boldsymbol{\epsilon}, \boldsymbol{\nu})$ can be divided into two parts, i.e. the elastic strain energy density $f_{\epsilon}(\boldsymbol{\phi}, \boldsymbol{\epsilon})$ and the kinetic energy density $f_{\nu}(\boldsymbol{\phi}, \boldsymbol{\nu})$. As a result, $f_{\epsilon}(\boldsymbol{\phi}, \boldsymbol{\epsilon})$ and $f_{\nu}(\boldsymbol{\phi}, \boldsymbol{\nu})$ are homogenized separately:

$$\begin{cases} f_{\epsilon}(\boldsymbol{\phi}, \boldsymbol{\epsilon}) = \sum_{\alpha}^N f_{\epsilon}^{\alpha}(\boldsymbol{\epsilon}^{\alpha}) h_{\alpha}(\boldsymbol{\phi}) \\ f_{\nu}(\boldsymbol{\phi}, \boldsymbol{\nu}) = \sum_{\alpha}^N f_{\nu}^{\alpha}(\boldsymbol{\nu}^{\alpha}) h_{\alpha}(\boldsymbol{\phi}) \end{cases} \quad (11)$$

Therefore, the effective stiffness matrix \mathbf{K} and the effective density matrix \mathcal{M} are derived to continuously and smoothly interpolate the elastic strain energy density $f_{\epsilon}(\boldsymbol{\phi}, \boldsymbol{\epsilon})$ and the kinetic energy density $f_{\nu}(\boldsymbol{\phi}, \boldsymbol{\nu})$, respectively. For the sake of completeness, the derivation procedure for \mathbf{K} and \mathcal{M} will be briefly reviewed in this section. For more details, please refer to [Liu et al. \(2021\)](#).

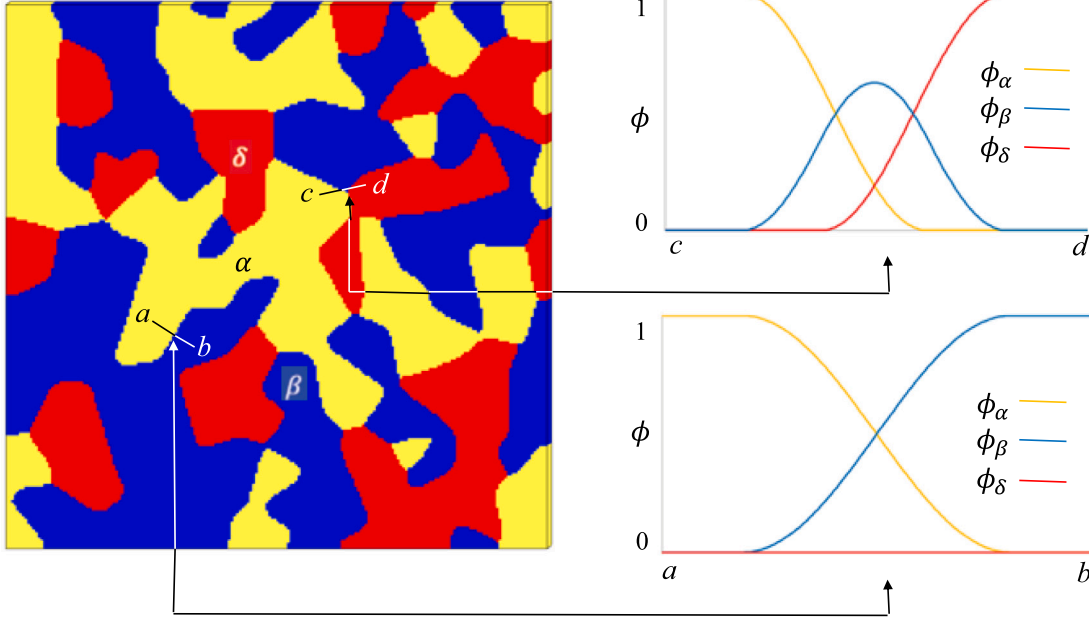


Fig. 1. Parametrization in a multiphase/multigrain system.

3.1. Effective stiffness matrix

Supposing that the base unit vectors $\{\xi, \eta, \zeta\} = \{(\xi_1, \xi_2, \xi_3)^\top, (\eta_1, \eta_2, \eta_3)^\top, (\zeta_1, \zeta_2, \zeta_3)^\top\}$ construct the local Cartesian coordinate system, with ξ as the vector normal to the interface and the superscript \top as the transpose operator, the local stress tensor in the Voigt notation $\tilde{\sigma} = (\sigma_{\xi\xi}, \sigma_{\eta\eta}, \sigma_{\zeta\zeta}, \sigma_{\eta\zeta}, \sigma_{\xi\zeta}, \sigma_{\xi\eta})^\top$ and the local strain tensor in the Voigt notation $\tilde{\varepsilon} = (\varepsilon_{\xi\xi}, \varepsilon_{\eta\eta}, \varepsilon_{\zeta\zeta}, \varepsilon_{\eta\zeta}, \varepsilon_{\xi\zeta}, \varepsilon_{\xi\eta})^\top$ can be respectively divided into the normal components $\tilde{\sigma}_n = (\sigma_{\xi\xi}, \sigma_{\xi\zeta}, \sigma_{\xi\eta})^\top$, $\tilde{\varepsilon}_n = (\varepsilon_{\xi\xi}, \varepsilon_{\xi\zeta}, \varepsilon_{\xi\eta})^\top$ and the tangential components $\tilde{\sigma}_t = (\sigma_{\eta\eta}, \sigma_{\zeta\zeta}, \sigma_{\eta\zeta})^\top$, $\tilde{\varepsilon}_t = (\varepsilon_{\eta\eta}, \varepsilon_{\zeta\zeta}, \varepsilon_{\eta\zeta})^\top$. According to the requirements of the force balance and the material continuity, the normal components of the stress tensor $\tilde{\sigma}_n$ and the tangential components of the strain tensor $\tilde{\varepsilon}_t$ are continuous across the interface (Schneider et al., 2015; Liu et al., 2021).

It is straightforward to obtain the relationship between the local Voigt notation stress/strain tensor and the global Voigt notation stress/strain tensor as $(\tilde{\sigma}_n, \tilde{\sigma}_t)^\top = \mathbf{M}_\sigma \sigma$ and $(\tilde{\varepsilon}_n, \tilde{\varepsilon}_t)^\top = \mathbf{M}_\varepsilon \varepsilon$, where the transformation matrices \mathbf{M}_σ and \mathbf{M}_ε are defined in Appendix. With $\mathbf{M}_\varepsilon^{-1} = \mathbf{M}_\sigma^\top$ and $\sigma = \bar{\mathbf{K}}\varepsilon$, it is derived for a single phase/grain that:

$$\begin{pmatrix} \tilde{\sigma}_n \\ \tilde{\sigma}_t \end{pmatrix} = \mathbf{M}_\sigma \bar{\mathbf{K}} \mathbf{M}_\sigma^\top \tilde{\varepsilon} = \tilde{\mathbf{K}} \tilde{\varepsilon} = \begin{pmatrix} \tilde{\mathbf{K}}^{11} & \tilde{\mathbf{K}}^{12} \\ \tilde{\mathbf{K}}^{21} & \tilde{\mathbf{K}}^{22} \end{pmatrix} \begin{pmatrix} \tilde{\varepsilon}_n \\ \tilde{\varepsilon}_t \end{pmatrix}, \quad (12)$$

where $\bar{\mathbf{K}}$ is the 6×6 stiffness matrix, $\tilde{\mathbf{K}}^{ij}$ ($i, j = 1, 2$) is the 3×3 submatrix in $\tilde{\mathbf{K}}$.

According to Eqs. (1), (10) and (11), the variational derivative of the elastic strain energy is expressed as:

$$\begin{aligned} \frac{\delta \int_V f_\varepsilon(\phi, \varepsilon) dV}{\delta \phi_\alpha} &= \frac{\partial f_\varepsilon(\phi, \varepsilon)}{\partial \phi_\alpha} = \frac{\partial \left(\sum_\beta f_L^\beta(\varepsilon^\beta) h_\beta(\phi) \right)}{\partial \phi_\alpha} \\ &= \sum_\beta f_L^\beta(\tilde{\sigma}_n, \tilde{\varepsilon}_t) \frac{\partial h_\beta(\phi)}{\partial \phi_\alpha}, \end{aligned} \quad (13)$$

where $f_L^\alpha(\tilde{\sigma}_n, \tilde{\varepsilon}_t)$ is the Legendre transform of the elastic strain energy density $f_\varepsilon^\alpha(\varepsilon^\alpha) = f_\varepsilon^\alpha(\mathbf{M}_\sigma^\top(\tilde{\varepsilon}_n, \tilde{\varepsilon}_t)^\top)$ with respect to $\tilde{\varepsilon}_n^\alpha$, which is expressed by the continuous components $\tilde{\sigma}_n$ and $\tilde{\varepsilon}_t$ as (Schneider et al., 2018):

$$f_L^\alpha(\tilde{\sigma}_n, \tilde{\varepsilon}_t) = \frac{1}{2} (\tilde{\sigma}_n, \tilde{\varepsilon}_t) \hat{\mathbf{K}}^\alpha \begin{pmatrix} \tilde{\sigma}_n \\ \tilde{\varepsilon}_t \end{pmatrix}, \quad (14)$$

where $\hat{\mathbf{K}}^\alpha$ is expressed as:

$$\begin{aligned} \hat{\mathbf{K}}^\alpha &= \begin{pmatrix} \hat{\mathbf{K}}^{11\alpha} & \hat{\mathbf{K}}^{12\alpha} \\ \hat{\mathbf{K}}^{21\alpha} & \hat{\mathbf{K}}^{22\alpha} \end{pmatrix} \\ &= \begin{pmatrix} -(\tilde{\mathbf{K}}^{11\alpha})^{-1} & (\tilde{\mathbf{K}}^{11\alpha})^{-1} \tilde{\mathbf{K}}^{12\alpha} \\ \tilde{\mathbf{K}}^{21\alpha} (\tilde{\mathbf{K}}^{11\alpha})^{-1} & (\tilde{\mathbf{K}}^{22\alpha} - \tilde{\mathbf{K}}^{21\alpha} (\tilde{\mathbf{K}}^{11\alpha})^{-1} \tilde{\mathbf{K}}^{12\alpha}) \end{pmatrix}. \end{aligned} \quad (15)$$

Since $\tilde{\sigma}_n$ and $\tilde{\varepsilon}_t$ are continuous across the interface, according to Eqs. (13) and (14), the elastic strain energy density $f_\varepsilon(\phi, \varepsilon)$ is expressed as:

$$\begin{aligned} f_\varepsilon(\phi, \varepsilon) &= \sum_\alpha f_L^\alpha(\tilde{\sigma}_n, \tilde{\varepsilon}_t) h_\alpha(\phi) = \frac{1}{2} (\tilde{\sigma}_n, \tilde{\varepsilon}_t) \sum_\alpha (\hat{\mathbf{K}}^\alpha h_\alpha(\phi)) \begin{pmatrix} \tilde{\sigma}_n \\ \tilde{\varepsilon}_t \end{pmatrix} \\ &= \frac{1}{2} (\tilde{\sigma}_n, \tilde{\varepsilon}_t) \hat{\mathbf{K}} \begin{pmatrix} \tilde{\sigma}_n \\ \tilde{\varepsilon}_t \end{pmatrix}. \end{aligned} \quad (16)$$

From Eq. (16), it is noticed that $(\tilde{\varepsilon}_n, \tilde{\sigma}_t)^\top = \hat{\mathbf{K}}(\tilde{\sigma}_n, \tilde{\varepsilon}_t)^\top$. By transforming this relationship back to the form of $(\tilde{\sigma}_n, \tilde{\sigma}_t)^\top = \tilde{\mathbf{K}}(\tilde{\varepsilon}_n, \tilde{\varepsilon}_t)^\top$, the following is obtained:

$$\tilde{\mathbf{K}} = \begin{pmatrix} -(\hat{\mathbf{K}}^{11})^{-1} & -(\hat{\mathbf{K}}^{11})^{-1} \hat{\mathbf{K}}^{12} \\ -\hat{\mathbf{K}}^{21} (\hat{\mathbf{K}}^{11})^{-1} & \hat{\mathbf{K}}^{22} - \hat{\mathbf{K}}^{21} (\hat{\mathbf{K}}^{11})^{-1} \hat{\mathbf{K}}^{12} \end{pmatrix}. \quad (17)$$

Thus, the effective stiffness matrix \mathbf{K} is derived from transforming $\tilde{\mathbf{K}}$ back to the global Cartesian coordinate system:

$$\mathbf{K} = \mathbf{M}_\varepsilon^\top \tilde{\mathbf{K}} \mathbf{M}_\varepsilon. \quad (18)$$

3.2. Effective density matrix

According to the requirement of material continuity, all the elements in the local velocity vector $\tilde{\mathbf{v}} = \{v_\xi, v_\eta, v_\zeta\}^\top$ are continuous across the interface (Liu et al., 2021). Supposing $\mathcal{M} = \text{diag}(\mathcal{M}_{11}, \mathcal{M}_{22}, \mathcal{M}_{33})$ is the density matrix in the global Cartesian coordinate system, the

density matrix in the local Cartesian coordinate system, i.e. $\widehat{\mathcal{M}}$, is calculated as:

$$\widehat{\mathcal{M}} = \mathbf{Q} \overline{\mathcal{M}} \mathbf{Q}^T, \quad (19)$$

where \mathbf{Q} is a transformation matrix, as defined in Appendix.

Based on Eqs. (1), (10) and (11), the variational derivative of the kinetic energy is:

$$\begin{aligned} \frac{\delta \left(\int_V f_v(\boldsymbol{\phi}, \mathbf{v}) dV \right)}{\delta \phi_\alpha} &= \frac{\partial f_v(\boldsymbol{\phi}, \mathbf{v})}{\partial \phi_\alpha} = \frac{\partial \left(\sum_\beta^N f_v^\beta(\mathbf{v}^\beta) h_\beta(\boldsymbol{\phi}) \right)}{\partial \phi_\alpha} \\ &= \sum_\beta^N f_v^\beta(\tilde{\mathbf{v}}) \frac{\partial h_\beta(\boldsymbol{\phi})}{\partial \phi_\alpha}. \end{aligned} \quad (20)$$

With $\tilde{\mathbf{v}} = \mathbf{Q}\mathbf{v}$, the kinetic energy density $f_v^\alpha(\mathbf{v}^\alpha)$ can be straightforwardly transformed into $f_v^\alpha(\tilde{\mathbf{v}})$. Therefore, the kinetic energy density $f_v(\boldsymbol{\phi}, \mathbf{v})$ is expressed as:

$$f_v(\boldsymbol{\phi}, \mathbf{v}) = \sum_\alpha^N f_v^\alpha(\tilde{\mathbf{v}}) h_\alpha(\boldsymbol{\phi}) = \frac{1}{2} \tilde{\mathbf{v}}^T \left(\widehat{\mathcal{M}}^\alpha h_\alpha(\boldsymbol{\phi}) \right) \tilde{\mathbf{v}} = \frac{1}{2} \tilde{\mathbf{v}}^T \widehat{\mathcal{M}} \tilde{\mathbf{v}}. \quad (21)$$

By transforming $\widehat{\mathcal{M}}$ from the local Cartesian coordinate system back to the global system, the effective density matrix \mathcal{M} is expressed as:

$$\mathcal{M} = \mathbf{Q}^T \widehat{\mathcal{M}} \mathbf{Q}. \quad (22)$$

It is noticed that the effective stiffness matrix combines the linear interpolation (VT model) and the harmonic interpolation (RS model), while the effective density matrix only employs the linear interpolation. By decomposing the interpolation scheme into the VT model and the RS model, with the derivation of the strain energy density and the complementary strain energy density, the advantage of the effective stiffness matrix \mathbf{K} is successfully avoiding the excessive elastic energy, which has been proven mathematically and numerically by Schneider et al. (2018). The proof procedure for the VT model can be straightforwardly applied to the effective density matrix \mathcal{M} , since linear interpolation is used for both of them.

4. Normal vector

From the formulas for the effective stiffness matrix \mathbf{K} and the effective density matrix \mathcal{M} in Section 3, it can be noticed that the foundation of the derivation procedure is to determine the normal vector $\boldsymbol{\xi}$ for the diffuse interface. For the interface generated by only two different phases/grains, i.e. α and β , the normal vector $\boldsymbol{\xi}$ is unique, since:

$$\boldsymbol{\xi} \equiv \frac{\nabla \phi_\alpha}{|\nabla \phi_\alpha|} \equiv - \frac{\nabla \phi_\beta}{|\nabla \phi_\beta|}. \quad (23)$$

However, when the interface is generated by more phases/grains, such as α, β, δ , the normal vector $\boldsymbol{\xi}$ becomes undetermined (Schneider et al., 2018), because the vectors $\nabla \phi_\alpha / |\nabla \phi_\alpha|, \nabla \phi_\beta / |\nabla \phi_\beta|, \nabla \phi_\delta / |\nabla \phi_\delta|$ are not always parallel to each other.

From the viewpoint of the obstacle or well type potential energy density in Eq. (3), the interface can be regarded as the result from the variation of:

$$M_{ob}(\boldsymbol{\phi}) = \sum_{\alpha, \beta > \alpha}^N \phi_\alpha \phi_\beta, \quad (24a)$$

$$M_{we}(\boldsymbol{\phi}) = \sum_{\alpha, \beta > \alpha}^N \phi_\alpha^2 \phi_\beta^2, \quad (24b)$$

while from the viewpoint of the material properties, i.e. the effective stiffness matrix \mathbf{K} and the effective density matrix \mathcal{M} , the interface is generated from the variation of:

$$M_{pr} = \sum_{\alpha, \beta > \alpha}^N \left(\frac{\sum_{i,j}^6 \llbracket K_{ij} \rrbracket^{\alpha\beta}}{\sum_{\alpha, \beta > \alpha}^N \left(\sum_{i,j}^6 \llbracket K_{ij} \rrbracket^{\alpha\beta} \right)} \right)$$

$$+ \frac{\sum_{i,j}^3 \llbracket \mathcal{M}_{ij} \rrbracket^{\alpha\beta}}{\sum_{\alpha, \beta > \alpha}^N \left(\sum_{i,j}^3 \llbracket \mathcal{M}_{ij} \rrbracket^{\alpha\beta} \right)} + \dots \Bigg) \phi_\alpha \phi_\beta, \quad (25)$$

where $\llbracket z \rrbracket^{\alpha\beta}$ represents the difference of the parameter z between the phases/grains α and β , and ... denotes the contribution from other factors which also play a role in generating the interface. When any denominator in Eq. (25) is equal to zero, the corresponding fraction term should be physically recognized as zero. Schneider et al. (2018) utilized the stiffness matrix and the nonelastic strain to determine M_{pr} .

As a consequence, the normal vector $\boldsymbol{\xi}$ can be calculated as:

$$\boldsymbol{\xi} = \frac{\nabla M_{ge}}{|\nabla M_{ge}|}, \quad (26)$$

where $M_{ge} = M_{ob}$ if considering Eq. (24a), while $M_{ge} = M_{pr}$ with Eq. (25). Eqs. (4), (24a) and (25) show that the normal vector $\boldsymbol{\xi}$ in Eq. (26) is equivalent to that in Eq. (23), when the diffuse interface is generated by only two different phases/grains.

Eqs. (24) and (25) show that M_{ob} and M_{we} are similar to each other, in comparison with M_{pr} . Therefore, M_{ob} is selected as a representative and is compared with M_{pr} in this paper. Fig. 2 illustrates an example for the interface generated by three phases/grains and the corresponding normal vector $\boldsymbol{\xi}$, calculated from Eqs. (24a) and (25), respectively. Here, the stiffness matrices $\overline{\mathbf{K}}^\alpha = \overline{\mathbf{K}}^\beta = \overline{\mathbf{K}}^\delta$, the density matrices $\overline{\mathcal{M}}^\alpha = 0.5\overline{\mathcal{M}}^\beta = 0.1\overline{\mathcal{M}}^\delta$ and the parameter $\epsilon = 5$. It is noticed that the three phases/grains are equally weighted in determining the normal vector $\boldsymbol{\xi}$ in Fig. 2(b), while the phase/grain δ plays a dominant role in Fig. 2(c), since $\overline{\mathcal{M}}^\delta$ is greater than $\overline{\mathcal{M}}^\alpha$ and $\overline{\mathcal{M}}^\beta$.

5. Mechanical wave

According to the continuity property of the mechanical wave, it can be divided into two different types, i.e. the Type I wave with strong discontinuity and the Type II with weak discontinuity (Liu et al., 2021; Wang, 2011). With $\mathbf{w} = \{w_1, w_2, w_3\}^T$ as the displacement field and Ω as the whole simulated domain, the Type I wave is defined as:

Definition 1. $\forall \epsilon > 0, \exists \delta_i > 0, \forall \mathbf{x} \in \Omega : |\mathbf{x} - \mathbf{x}_0| < \delta_i \implies |w_i(\mathbf{x}, t) - w_i(\mathbf{x}_0, t)| < \epsilon \quad (i = 1, 2, 3; \mathbf{x}_0 \in \Omega; t > 0)$.

Definition 1 means that the displacement field \mathbf{w} of the Type I wave is continuous within the whole domain Ω , which is also essential to satisfy the requirement of material continuity. On the basis of Definition 1 and with further constraints, the definition of the Type II wave is given as:

Definition 2. $\forall \epsilon > 0, \exists \delta_{1ij}, \delta_{2i} > 0 :$

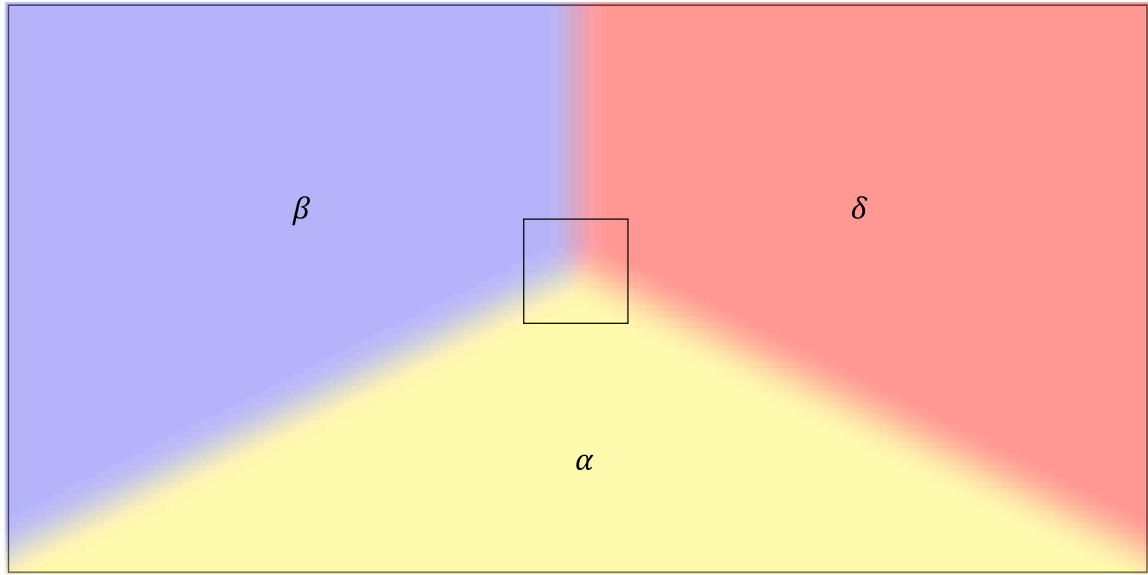
$$\begin{aligned} (1) \quad \forall \mathbf{x} \in \overline{\Omega}_\alpha, \|\mathbf{x} - \mathbf{x}_0\|_2 < \delta_{1ij} &\implies \left| \frac{\partial w_i(\mathbf{x}, t)}{\partial x_j} - \frac{\partial w_j(\mathbf{x}, t)}{\partial x_i} \right|_{\mathbf{x}=\mathbf{x}_0} < \epsilon, \\ (2) \quad \forall t > 0, |t - t_0| < \delta_{2i} &\implies \left| \frac{\partial w_i(\mathbf{x}, t)}{\partial t} - \frac{\partial w_j(\mathbf{x}, t)}{\partial t} \right|_{t=t_0} < \epsilon, \quad (i, j = 1, 2, 3; \mathbf{x}, \mathbf{x}_0 \in \overline{\Omega}_\alpha, t, t_0 > 0), \end{aligned}$$

where $\overline{\Omega}_\alpha$ refers to the domain containing only the phase/grain α . Definition 2 demonstrates that both the first order spatial and temporal derivations of the displacement field \mathbf{w} are continuous within the domain $\overline{\Omega}_\alpha$. Fig. 3 exemplifies a waveform for the Type I and the Type II wave.

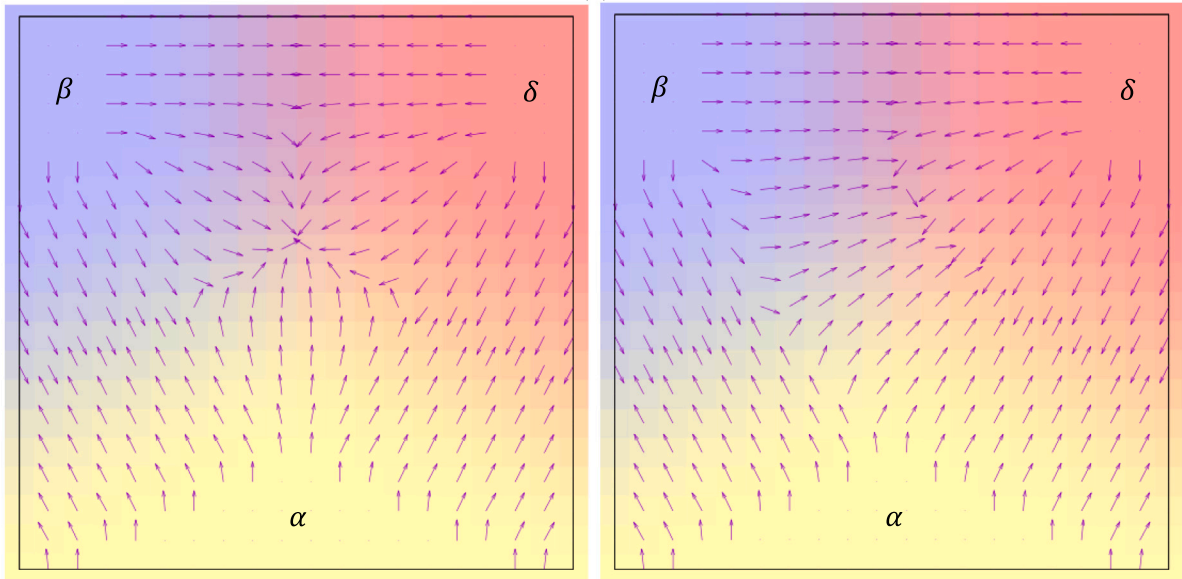
6. Solver for mechanical wave propagation

Originated from the wave equation:

$$\ddot{w}_i(\mathbf{x}, t) = \frac{1}{\rho} \sigma_{ij,j}(\mathbf{x}, t) + f_i(\mathbf{x}, t) \quad (i, j = 1, 2, 3), \quad (27)$$



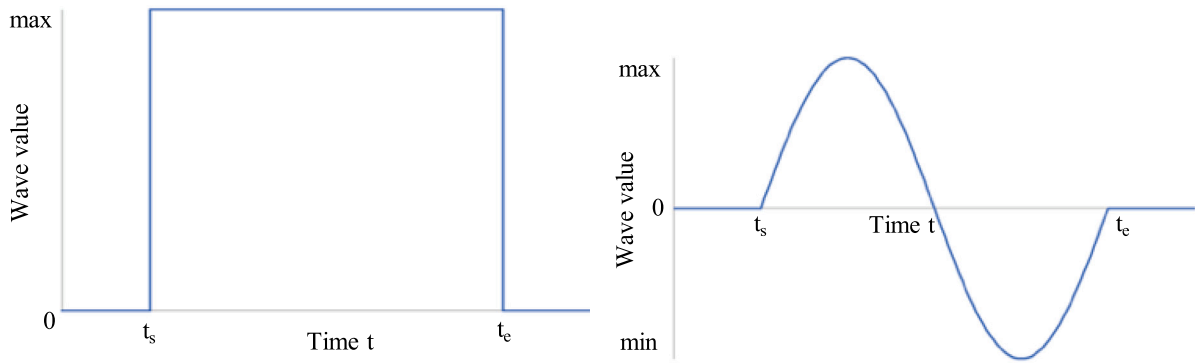
(a)



(b)

(c)

Fig. 2. (a) An example for the interface generated in a three-phase/grain region, (b) and (c): normal vector representation for the domain within the central square, according to Eq. (24a) and Eq. (25), respectively.



(a)

(b)

Fig. 3. The examples for the (a) Type I and (b) Type II wave (t_s and t_e respectively represent the beginning and the end of the incident wave).

and the constitutive equation:

$$\sigma_i(\mathbf{x}, t) = K_{ij} \varepsilon_j(\mathbf{x}, t) \quad (i, j = 1, 2, \dots, 6), \quad (28)$$

the governing equations for mechanical wave propagation can be expressed in the form of stress and velocity (LeVeque et al., 2002):

$$\dot{u}_i(\mathbf{x}, t) = C_{ij}^k u_{j,k}(\mathbf{x}, t) + s_i(\mathbf{x}, t) \quad (i, j = 1, 2, \dots, 9; k = 1, 2, 3), \quad (29)$$

where $\ddot{w}_i = \partial^2 w_i / \partial t^2$ and $\sigma_{ij,j} = \partial \sigma_{ij} / \partial x_j$ respectively are the second order temporal derivation of the displacement $w_i(\mathbf{x}, t)$ and the first order spatial derivation of the stress $\sigma_{ij}(\mathbf{x}, t)$. ρ denotes the density of materials, and $f_i(\mathbf{x}, t)$ represents the mechanical wave source. σ_i is the i th element in the Voigt notation stress tensor $\boldsymbol{\sigma} = (\sigma_{11}, \sigma_{22}, \sigma_{33}, \sigma_{23}, \sigma_{13}, \sigma_{12})^\top$, while ε_j denotes the j th element in the Voigt notation strain tensor $\boldsymbol{\varepsilon} = (\varepsilon_{11}, \varepsilon_{22}, \varepsilon_{33}, \varepsilon_{23}, \varepsilon_{13}, \varepsilon_{12})^\top$. $u_i(\mathbf{x}, t)$ represents the i th element in the vector $\mathbf{u} = (\sigma_{11}, \sigma_{22}, \sigma_{33}, \sigma_{23}, \sigma_{13}, \sigma_{12}, v_1, v_2, v_3)^\top$, where $\mathbf{v} = (v_1, v_2, v_3)$ is the material particle velocity vector. C_{ij}^k is the element in the i th row and the j th column of the coefficient matrix \mathbf{C}^k , which is provided in Appendix. $s_i(\mathbf{x}, t)$ denotes the mechanical wave source corresponding to $u_i(\mathbf{x}, t)$.

For each cubic cell ζ , a vector \mathbf{u}^ζ is assigned and approximated by a series of orthogonal polynomials:

$$u_i^\zeta(\mathbf{x}, t) = a_{ij}^\zeta(t) p_j(\mathbf{x}) \quad (j = 1, 2, \dots, N_q). \quad (30)$$

Here the unknown $a_{ij}^\zeta(t)$ is dependent on the time t , and $N_q = (q+1)(q+2)(q+3)/6$, with q as the highest polynomial degree in Eq. (30). The polynomial $p_j(\mathbf{x})$ is orthogonal, by satisfying the following constraint:

$$\int_{V_\zeta} p_{j_1}(\mathbf{x}) p_{j_2}(\mathbf{x}) dV_\zeta = \begin{cases} 1 & (j_1 = j_2) \\ 0 & (j_1 \neq j_2), \end{cases} \quad (31)$$

where V_ζ represents the volume of the cell ζ .

According to Taylor's theorem, the mechanical wave source $s_i^\zeta(\mathbf{x}, t)$ can also be approximated by a series of orthogonal polynomials:

$$s_i^\zeta(\mathbf{x}, t) = b_{ij}^\zeta(t) p_j(\mathbf{x}), \quad (32)$$

where $b_{ij}^\zeta(t)$ is calculated from the Taylor series of the mechanical wave source $s_i^\zeta(\mathbf{x}, t)$ and the polynomial series $p_j(\mathbf{x})$.

On the basis of Eqs. (30), (31) and (32), the weak form of Eq. (29) can be constructed as:

$$\int_{V_\zeta} \dot{u}_i^\zeta(\mathbf{x}, t) p_l(\mathbf{x}) dV_\zeta = C_{ij}^{k\zeta} \int_{V_\zeta} u_{j,k}^\zeta(\mathbf{x}, t) p_l(\mathbf{x}) dV_\zeta + \int_{V_\zeta} s_i^\zeta(\mathbf{x}, t) p_l(\mathbf{x}) dV_\zeta, \quad (33)$$

for the cell ζ .

According to the product rule of the derivation, the divergence theorem, the upwind Riemann solver and the forward finite difference approximation, the solution for Eq. (33) is (Liu et al., 2021; Käser and Dumbser, 2006):

$$\begin{aligned} a_{il}^\zeta(t + \Delta t) = & a_{il}^\zeta(t) + \Delta t \left(\frac{1}{2} \int_{S_\zeta} T_{ij}^{S_\zeta} (C_{jm}^{k\zeta} - D_{jm}^{k\zeta}) \right. \\ & \times (T^{S_\zeta})_{mr}^{-1} a_{rs}^\zeta(t) p_s(\mathbf{x}) p_l(\mathbf{x}) dS_\zeta + \\ & \left. \frac{1}{2} \int_{S_\zeta} T_{ij}^{S_\zeta} (C_{jm}^{k\zeta} + D_{jm}^{k\zeta}) (T^{S_\zeta})_{mr}^{-1} a_{rs}^{\zeta S_\zeta}(t) p_s(\mathbf{x}) p_l(\mathbf{x}) dS_\zeta - \right. \\ & \left. C_{ij}^{k\zeta} \int_{V_\zeta} a_{jm}^\zeta(t) p_m(\mathbf{x}) p_{l,k}(\mathbf{x}) dV_\zeta + b_{il}^\zeta(t) \right) \end{aligned} \quad (34)$$

where Δt is the timestep for the temporal discretization, and S_ζ represents the surface of the cell ζ . T^{S_ζ} denotes the transformation matrix, which is defined in the Appendix with the vector $\boldsymbol{\xi}$ normal to the

Table 2

The normalized material properties for the phase/grain β .

Property	R_K^β					R_ρ^β				
Fixed density	0.1	0.5	1	2	10					1
Fixed stiffness			1			0.1	0.5	1	2	10

surface S_ζ . $a_{rs}^{\zeta S_\zeta}$ refers to the unknown of the cell which shares the surface S_ζ with the cell ζ . The matrix $\mathbf{D}^{k\zeta}$ is calculated as:

$$D_{ij}^{k\zeta} = G_{il}^{k\zeta} H_{lm}^{k\zeta} (G^{k\zeta})_{mj}^{-1}, \quad (35)$$

where the Einstein summation convention does not apply to the super script k . The matrix $\mathbf{H}^{k\zeta} = \text{diag}(|h_1|, |h_2|, \dots, |h_9|)$, with h_i ($i = 1, 2, \dots, 9$) as the eigenvalue of the matrix $\mathbf{C}^{k\zeta}$ and $h_{i_1} \leq h_{i_2}$ ($i_1 < i_2$). The matrix $\mathbf{G}^{k\zeta} = (\mathbf{g}_1, \mathbf{g}_2, \dots, \mathbf{g}_9)$, and the vector \mathbf{g}_i ($i = 1, 2, \dots, 9$) is the right eigenvector of the matrix $\mathbf{C}^{k\zeta}$, corresponding to the eigenvalue h_i .

By substituting Eq. (34) into Eq. (30), the stress and velocity fields can be obtained. With the effective stiffness matrix \mathbf{K} and the effective density matrix \mathcal{M} , the strain and momentum fields can be derived. Thus, the elastic strain energy density f_ε , the kinetic energy density f_v and the dynamic mechanical energy density f_d can be easily calculated. Based on the initial state of the displacement field and the integration of the velocity field over time, the displacement field occurring during the process of the numerical simulation can be obtained.

7. Numerical simulation

In this section, the dynamic mechanical energy is analysed for the Types I and II wave. In Sections 7.1 and 7.2, parameter studies are carried out considering the stiffness matrix, the density and the phase/grain size. A detailed comparison between Eqs. (24a) and (25) is presented in Section 7.3. In Sections 7.1 and 7.3, the numerical results are also compared with those from the linear homogenization method, i.e. the VT model. For all numerical examples in this section, the polynomial degree q in Eq. (30) is fixed as 3.

7.1. Influence of stiffness and density

A numerical example containing two phases/grains, i.e. α and β , is demonstrated in Fig. 4. The simulated domain with the dimension of $1 \mu\text{m} \times 200 \mu\text{m} \times 100 \mu\text{m}$ is discretized into 20000 cells, each of which is $1 \mu\text{m} \times 1 \mu\text{m} \times 1 \mu\text{m}$. In this subsection, the radius of the β phase/grain is fixed as $10 \mu\text{m}$, which occupies 1.57% of the total volume. The origin of the global Cartesian coordinate system is located at the left bottom back corner of the simulated domain, with the x_2 axis pointing to the right side and x_3 to the top side. Fig. 4 can be treated as a 2D example, with the surfaces normal to x_2 and x_3 as free boundaries. The one cycle Types I and II incident wave with the frequency of 50 MHz are applied at the centre of the bottom boundary, i.e. upon the area $[(0, 100, 0), (1, 101, 0)]$. The stress amplitude is designed as $|\sigma|_{\max} = 100 \text{ MPa}$. For the convenience of analysis, the stiffness and the density for each phase/grain are designed proportional to those for the phase/grain α . For instance, the stiffness and density for the phase/grain β are:

$$\overline{\mathbf{K}}^\beta = R_K^\beta \overline{\mathbf{K}}^\alpha, \quad \overline{\mathcal{M}}^\beta = R_\rho^\beta \overline{\mathcal{M}}^\alpha, \quad (36)$$

where R_K^β and R_ρ^β respectively are the stiffness ratio and the density ratio for the phase/grain β . In this subsection, the material properties for the phase/grain β are listed in Table 2. For the cases with a fixed density ratio, i.e. $R_\rho^\beta = 1$, the stiffness ratio R_K^β ranges from 0.1 to 10. For the other cases, the stiffness ratio $R_K^\beta = 1$, while the density ratio varies from 0.1 to 10.

The numerical example in Fig. 4 is firstly simulated with a sharp interface between the phases/grains α and β , whose results provide

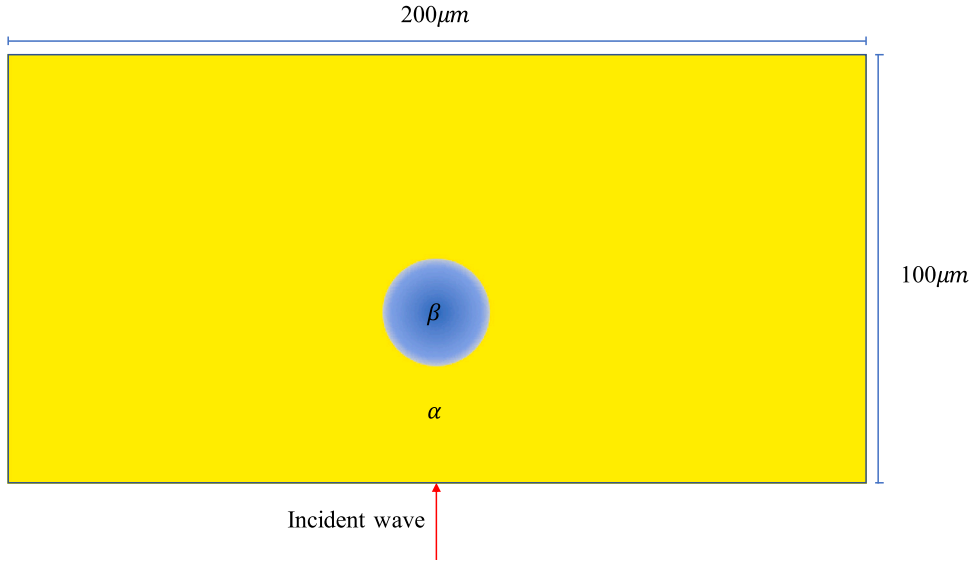


Fig. 4. A numerical example with one inner phase/grain.

a benchmark to analyse the numerical results from the corresponding diffuse interface case.

By comparing with the total mechanical energy at the end of loading, i.e. at $t = 20$ ns, the numerical error for a period of 60 ns, after the end of loading, is presented in Fig. 5. It is observed that the error for the Type II wave is less than 0.3%, which is negligible. However, the error for the Type I wave converges to the values around 7.5%. Therefore, it can be concluded that the numerical error in the Type I wave case is mainly caused by its property of strong discontinuity, as defined in Definition 1 and shown in Fig. 3(a). It is impossible for the numerical results to exactly reproduce the sharp jump of the waveform. When approximating the Type I wave with high order polynomials, there are fluctuations at the beginning and end of the waveform (Liu et al., 2021), where the sharp jump exists. As a result, the total mechanical energy becomes greater than the exact value. During the process of wave propagation, transmission and reflection, the mechanical energy disperses, which results in a lower fluctuation amplitude and a decrease of total mechanical energy. Gradually, the total mechanical energy tends to be constant, as illustrated in Figs. 5(a) and 5(b).

In Fig. 5, it is also noticed that the numerical errors for different stiffness/density ratios deviate differently from the case with $R_K^\beta = R_\rho^\beta = 1$, i.e. the red curves in Fig. 5. For the case with the Type I wave, i.e. Figs. 5(a) and 5(b), the deviation is mainly caused due to two different reasons. For the cases with $R_K^\beta = 10$ and $R_\rho^\beta = 0.1$, the wave propagation velocity in the phase/grain α is the lowest. As a consequence, the numerical error converges at a slower rate, compared with other cases. For the cases with $R_\rho^\beta = 10$ and with $R_\rho^\beta = 2$, the reflected wave energy, which is caused by the interface between the phases/grains α and β , arrives at the bottom boundary before the end of loading. At this time, the reflected stress is pressure, and the loading force is in the positive direction of the x_3 axis. Since the total stress at the loading boundary is kept as a pressure of 100 MPa, the mechanical energy flowing into the simulated domain is decreased. Therefore, the percentage of the non physical excess energy, which is contributed by the mathematical fluctuation at the sharp jump, increases. As a result, the corresponding numerical error in figure 5(b) converges to a greater value. For the case with the Type II wave, i.e. Figs. 5(c) and 5(d), almost all cases converge to a small value around 0.2%, because the stress/velocity waveform is continuous. However, the error tends to be smaller when $R_K^\beta = 10$ or $R_\rho^\beta = 0.1$, since the wave propagation velocity in phase/grain α is smallest under this condition.

The percentage of mechanical energy within the phase/grain α is plotted in Fig. 6. For the convenience of analysis, the transmission ratio

of the mechanical energy under the condition of R_K^β or R_ρ^β , i.e. $R_{R_K^\beta}^{eK}$ or $R_{R_\rho^\beta}^{e\rho}$, is defined as:

$$R_{R_K^\beta}^{eK} = \frac{E^t_{R_K^\beta}}{E^t_{R_K^\beta} + E^r_{R_K^\beta}}, \quad R_{R_\rho^\beta}^{e\rho} = \frac{E^t_{R_\rho^\beta}}{E^t_{R_\rho^\beta} + E^r_{R_\rho^\beta}}, \quad (37)$$

where $E^t_{R_K^\beta}$ and $E^r_{R_K^\beta}$ respectively represent the transmitted energy and the reflected energy, when the mechanical energy flows from the phase/grain α to the phase/grain β , under the condition of R_K^β . A similar definition applies to $E^t_{R_\rho^\beta}$ and $E^r_{R_\rho^\beta}$. Since the geometrical condition is fixed in this example, it is not difficult to obtain that $R_1^{eK} > R_{0.5}^{eK} > R_{0.1}^{eK}$ and $R_1^{e\rho} > R_2^{e\rho} > R_{10}^{e\rho}$ when R_ρ^β is fixed as 1, and that $R_1^{e\rho} > R_{0.5}^{e\rho} > R_{0.1}^{e\rho}$ and $R_1^{eK} > R_2^{eK} > R_{10}^{eK}$ when $R_K^\beta = 1$ holds. For both the Types I and II wave in Fig. 6, it can be observed that the energy percentage for $R_K^\beta = 1, 2, 10$ and $R_\rho^\beta = 0.1, 0.5, 1$ satisfies the aforementioned inequation about the transmission ratio. For the other cases, the wave propagation velocity within the phase/grain β is assigned with a smaller value. Specifically, $V_{0.1}^{\beta K} < V_{0.5}^{\beta K} < V_1^{\beta K} = V_2^{\beta K} = V_{10}^{\beta K}$ and $V_{10}^{\beta\rho} < V_2^{\beta\rho} < V_1^{\beta\rho} = V_{0.5}^{\beta\rho} = V_{0.1}^{\beta\rho}$, supposing that $V_a^{\beta b}$ denotes the P/S wave (primary/secondary wave) propagation velocity under the condition of $R_b^\beta = a$. Therefore, more mechanical energy can be preserved within the phase/grain β , before it is transmitted into the phase/grain α through the upper half interface. As a result, the energy percentage within the phase/grain α becomes smaller. It is also noticed that the energy percentage for the case of $R_\rho^\beta = 10$, i.e. the green curves in Figs. 6(b) and 6(d), decreases more compared to the other cases. This is also due to the reason that the total mechanical energy, specifically the energy within the phase/grain α , decreases, similar to the cases $R_\rho^\beta = 10$ and $R_\rho^\beta = 2$ in Fig. 5(b). This decrease is enlarged in Fig. 6(d), because an energy crest is transmitted from the phase/grain α into the phase/grain β .

Then, the sharp interface is replaced by a diffuse interface with $\epsilon = 5$, and the numerical results from the diffuse interface case are compared with those from the sharp interface case. The numerical errors of the total mechanical energy and of the energy percentage for the phase/grain α are respectively illustrated in Figs. 7 and 8. It is observed that the numerical errors for all cases are less than 3%. For most cases, the error converges to the value of less than 0.5%.

In Fig. 7, the error is mainly generated before the end of loading, i.e. $t \leq 20$ ns, after which the error tends to be stable. Therefore, it can be concluded that the error is caused by a wider interface, which leads

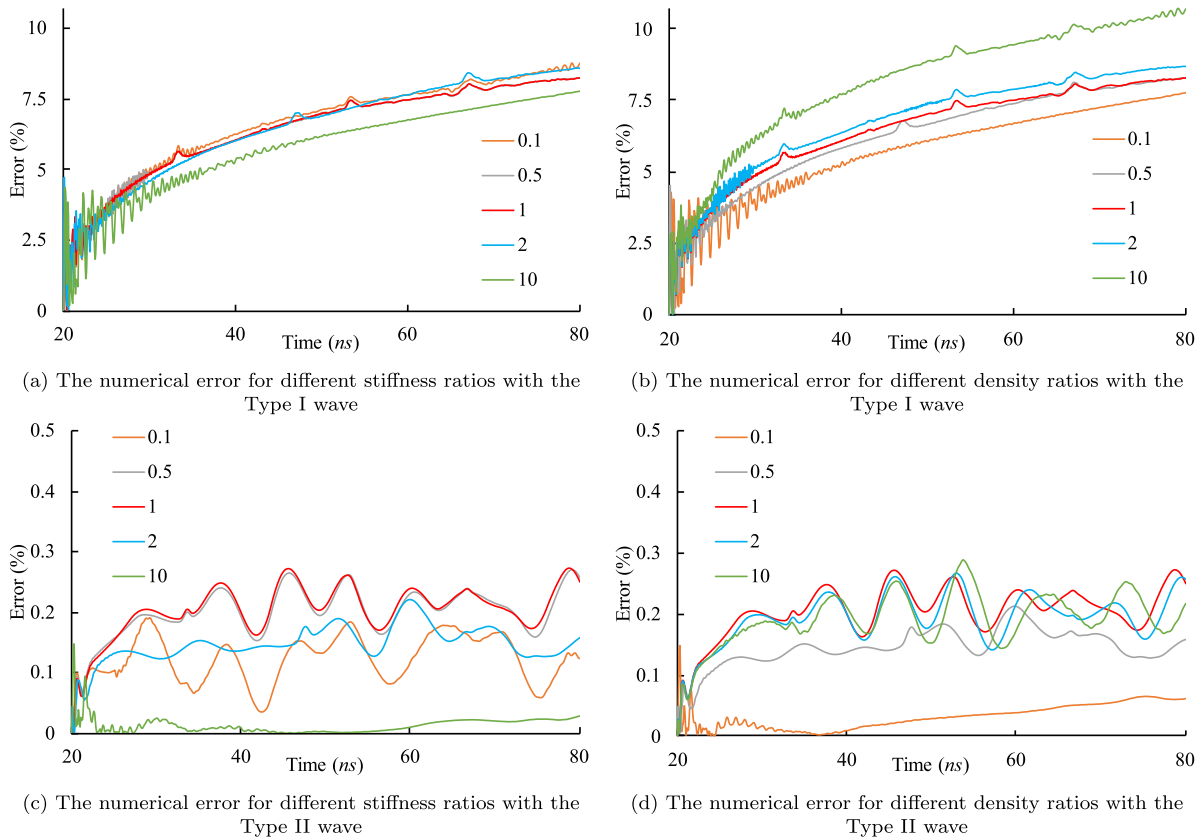


Fig. 5. The numerical error of the total mechanical energy for the case with a sharp interface.

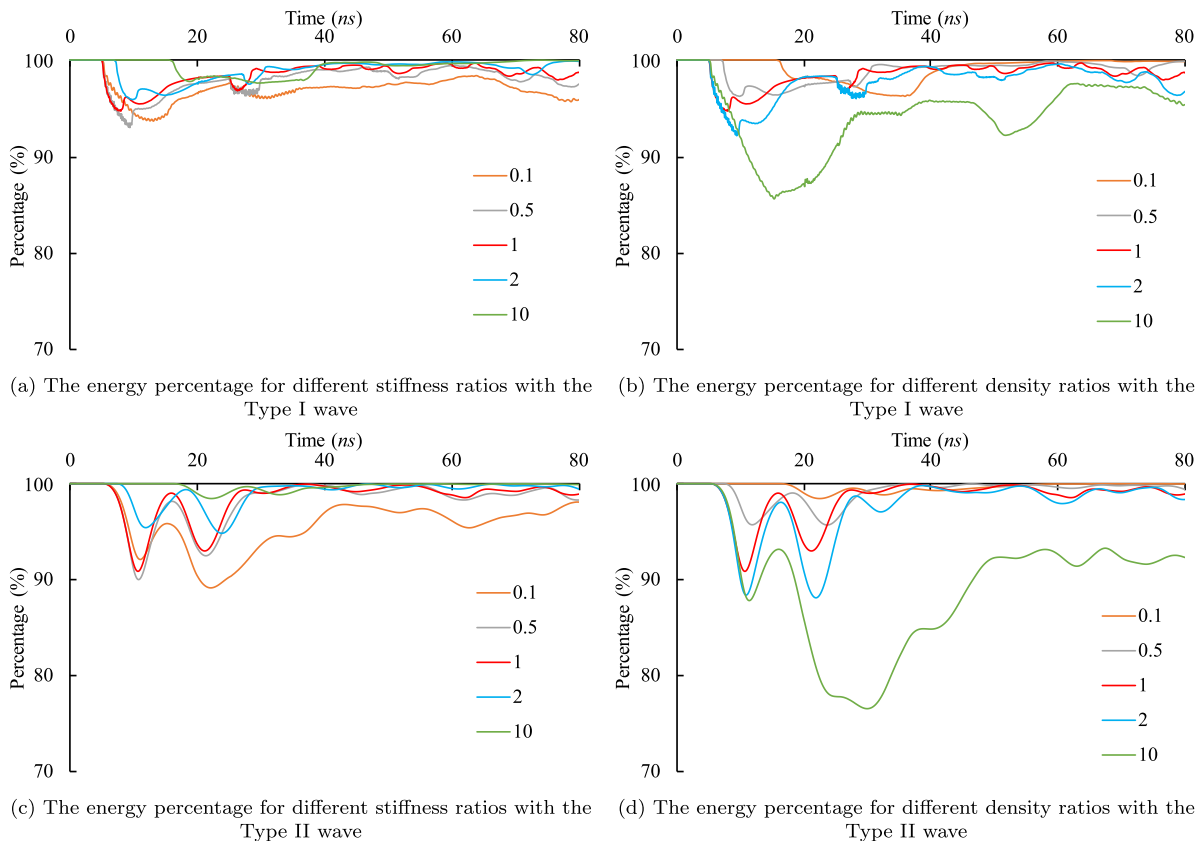


Fig. 6. The percentage of mechanical energy within the phase/grain α , for the case with a sharp interface.

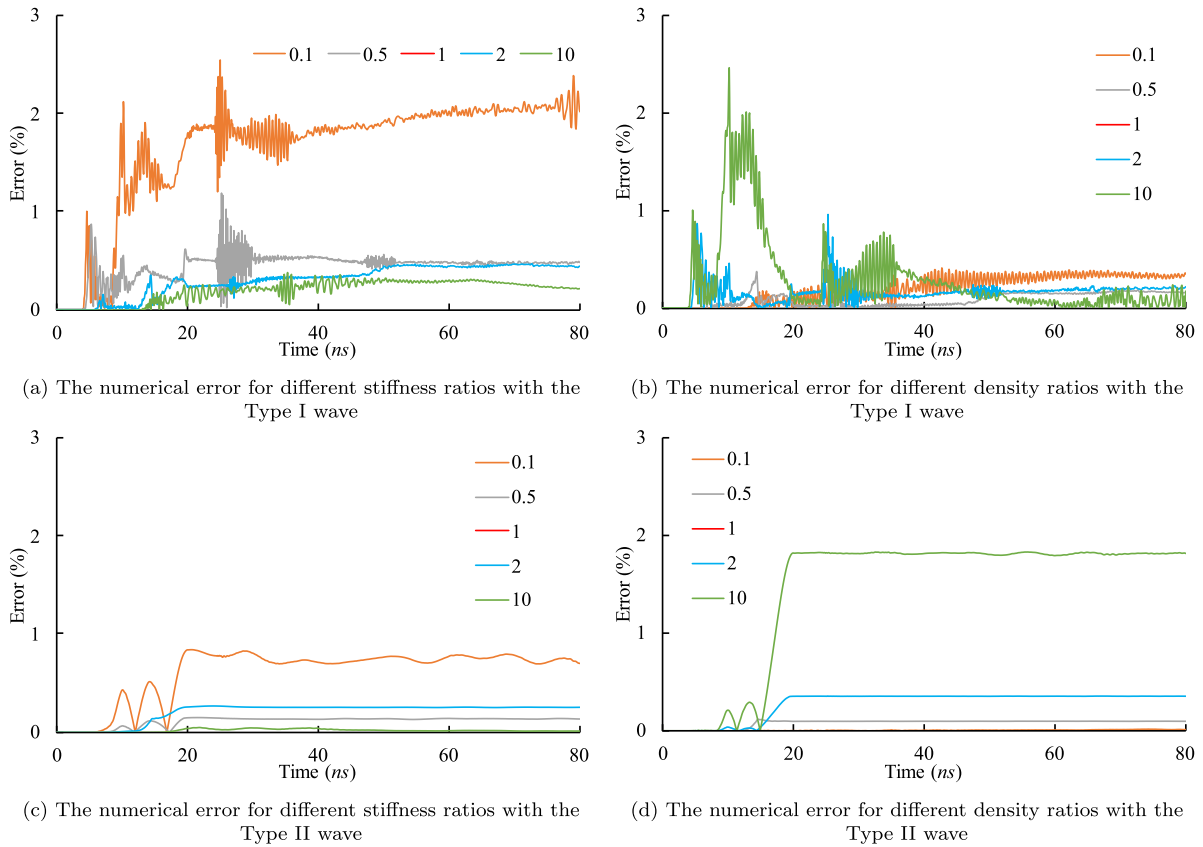


Fig. 7. The numerical error of the total mechanical energy caused by replacing the sharp interface with a diffuse interface.

to an earlier energy reflection. Since the reflected energy arrives at the loading boundary earlier, the influence of the loading condition upon the total mechanical energy is enhanced. This influence disappears after the end of loading, i.e. $t > 20$ ns. The difference of the errors in Fig. 7 is caused by the difference of the total energy, of the reflected energy density, of the wave propagation velocity in the phase/grain α , of the reflected stress and of the waveform.

In Fig. 8, the numerical error fluctuates more frequently than in Fig. 7. This is due to the frequent wave transmission and reflection at the interface. For an incident wave, the wave reflection begins earlier and ends later in the diffuse interface case. This is also observed in Liu et al. (2021). After an incident wave completely passes through the diffuse interface, the energy percentage within each phase/grain becomes the same as in the sharp interface case. In this example, the mechanical wave passes through the interface frequently, since the interface is a circle. As a result, the fluctuation of the numerical error exists all the time in Fig. 8. However, the error is negligible overall, as it is less than 0.5% in most cases.

For the Type I wave with $R_p^\beta = 10$ at $t = 60$ ns and the Type II wave with $R_K^\beta = 0.1$ at $t = 40$ ns, the energy density from the diffuse interface case is compared with the sharp interface case, as illustrated in Fig. 9. Generally, the numerical results from the diffuse and sharp interface cases agree well with each other for both wave types. Moreover, the energy density is smoothly diffused at the interface in Figs. 9(a) and 9(c).

With the stiffness ratio varying from 0.1 to 10, the homogenization scheme for the effective stiffness matrix in Section 3.1 is compared with the linear homogenization method, i.e. the VT model, through the difference of the numerical errors, as illustrated in Fig. 10. The error difference is equal to $E_l - E_p$, with E_l and E_p respectively representing the error of the linear homogenization scheme and of the proposed homogenization scheme. Therefore, when the error difference is positive, the proposed homogenization method performs better, and

vice versa. Figs. 10(a) and 10(c) respectively demonstrate the error difference for the total mechanical energy with the Types I and II wave, while Figs. 10(b) and 10(d) respectively show the percentages of the positive/negative error difference for the mechanical energy within the phase/grain α . It is observed that the proposed homogenization scheme generally performs better than the linear homogenization method.

7.2. Influence of phase/grain size

In this subsection, the numerical example in Fig. 4 is re simulated with the Type II wave. According to the material properties, the numerical results can be categorized into two groups. In the first group, $R_K^\beta = 0.2$ and $R_p^\beta = 1$, while $R_K^\beta = 1$ and $R_p^\beta = 5$ in the second group. In each group, the radius of the phase/grain β ranges from 5 to 20.

The interface is firstly designed as a sharp interface, similar to Section 7.1. In Fig. 11, the numerical error of the total mechanical energy is illustrated for a period of 60 ns after the end of loading. For all cases, the error is around 0.25%, which is negligible. The percentage of mechanical energy within the phase/grain α is shown in Fig. 12. It is observed that the energy percentage decreases, when the radius of the phase/grain β increases. For each case in Fig. 12(a), the energy percentage is less than the corresponding case in Fig. 12(b), because the loading force is tension, when the reflected energy, which results from the interface between the phases/grains α and β , arrives at the loading boundary. For $R_K^\beta = 0.2$, the reflected stress is pressure, while for $R_p^\beta = 5$, it is tension. Since the total stress at the loading boundary is kept as a sinusoid, the total mechanical energy flowing into the simulated domain, specifically into the phase/grain α , becomes greater for $R_K^\beta = 0.2$ and lower for $R_p^\beta = 5$, in comparison with the case $R_K^\beta = R_p^\beta = 1$. As a result, the energy percentage within the phase/grain α is lower in Fig. 12(a) and higher in 12(b).

For the case with a diffuse interface, the total mechanical energy and the energy percentage within the phase/grain α are compared with

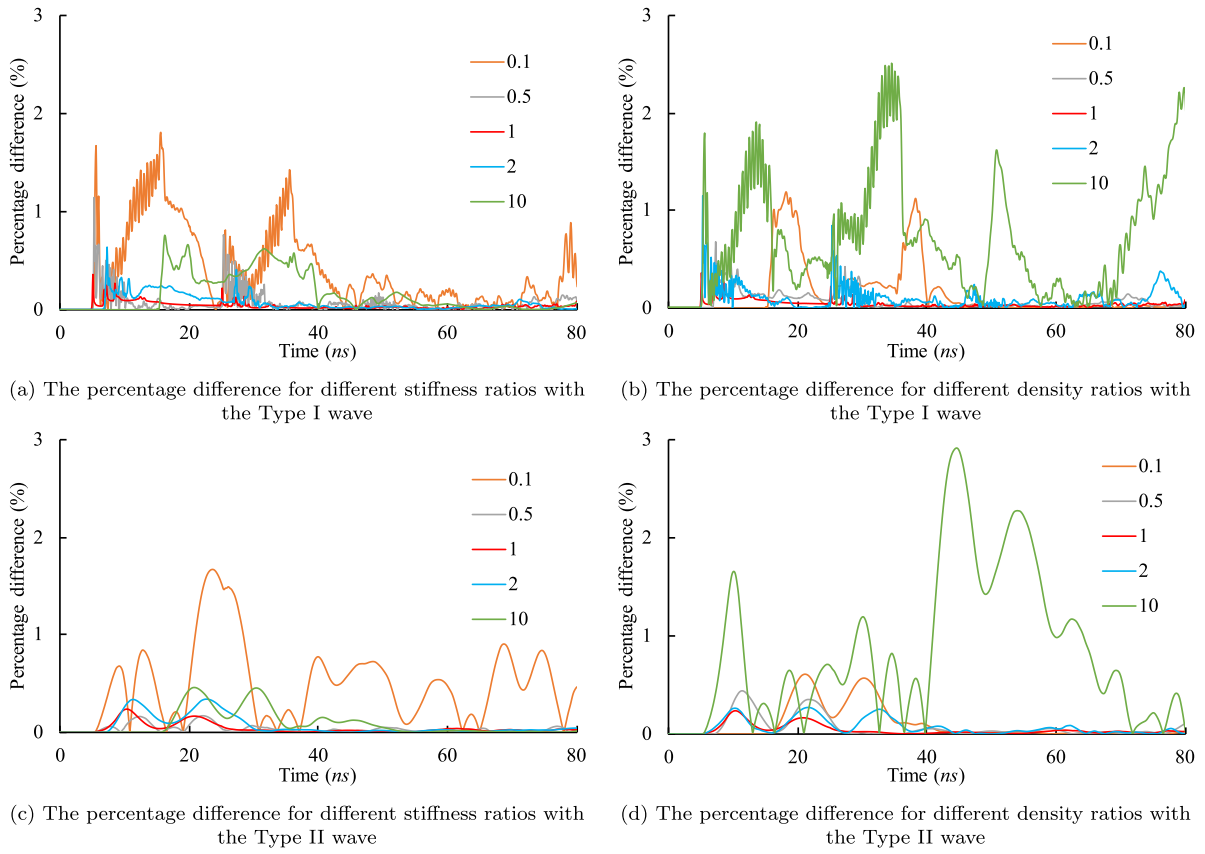


Fig. 8. The difference of the energy percentage within the phase/grain α , between the cases with a sharp interface and a diffuse interface.

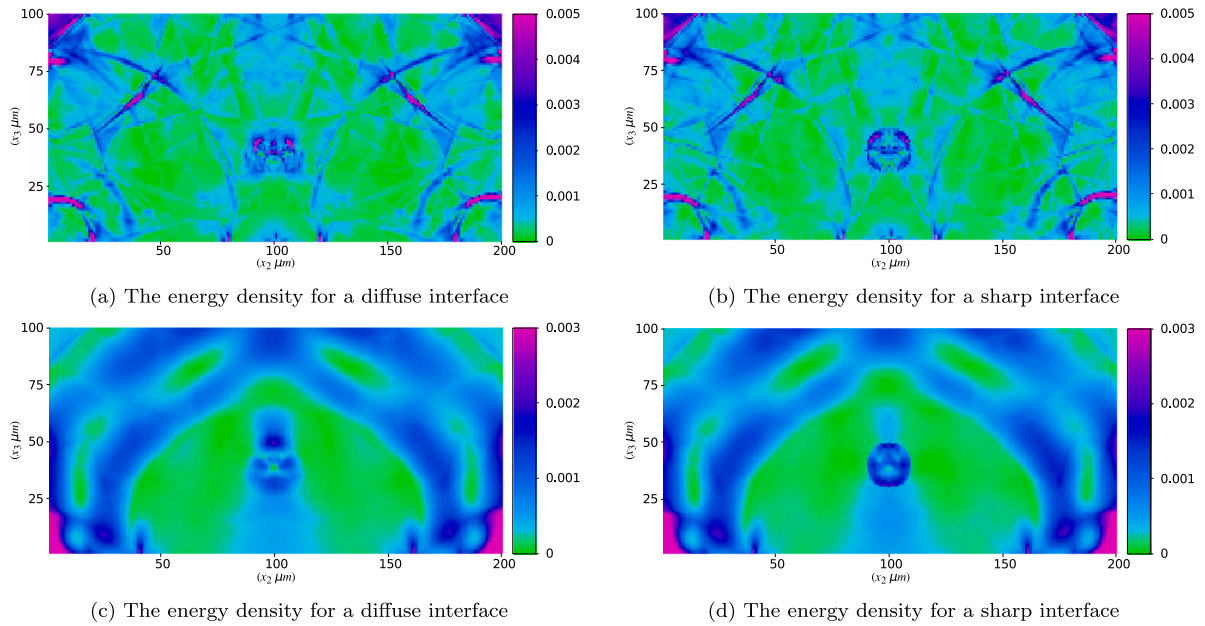


Fig. 9. The mechanical energy density for (a) and (b): the density ratio $R_p^\beta = 10$ and time $t = 60$ ns with the Type I wave, for (c) and (d): the stiffness ratio $R_k^\beta = 0.1$ and time $t = 40$ ns with the Type II wave (unit: $10E+04$ J/m³).

those from the sharp interface case, as shown in Figs. 13 and 14. In general, as the radius of the phase/grain β increases, the numerical error increases as well. However, it is less than 2% for almost all cases. In Fig. 13, the error is mainly generated before the end of loading. This means that the error is also caused by an earlier wave reflection at the diffuse interface, similar to Fig. 7. When the radius of phase/grain β

increases, the reflected energy increases, which leads to a larger error in Fig. 13. However, since the total stress at the loading boundary is fixed as 100 MPa, the error tends to converge when increasing the radius. In Fig. 14, the fluctuation phenomenon is similar to Fig. 8. When the radius increases, the domain for the diffuse interface becomes larger, which results in a greater error fluctuation.

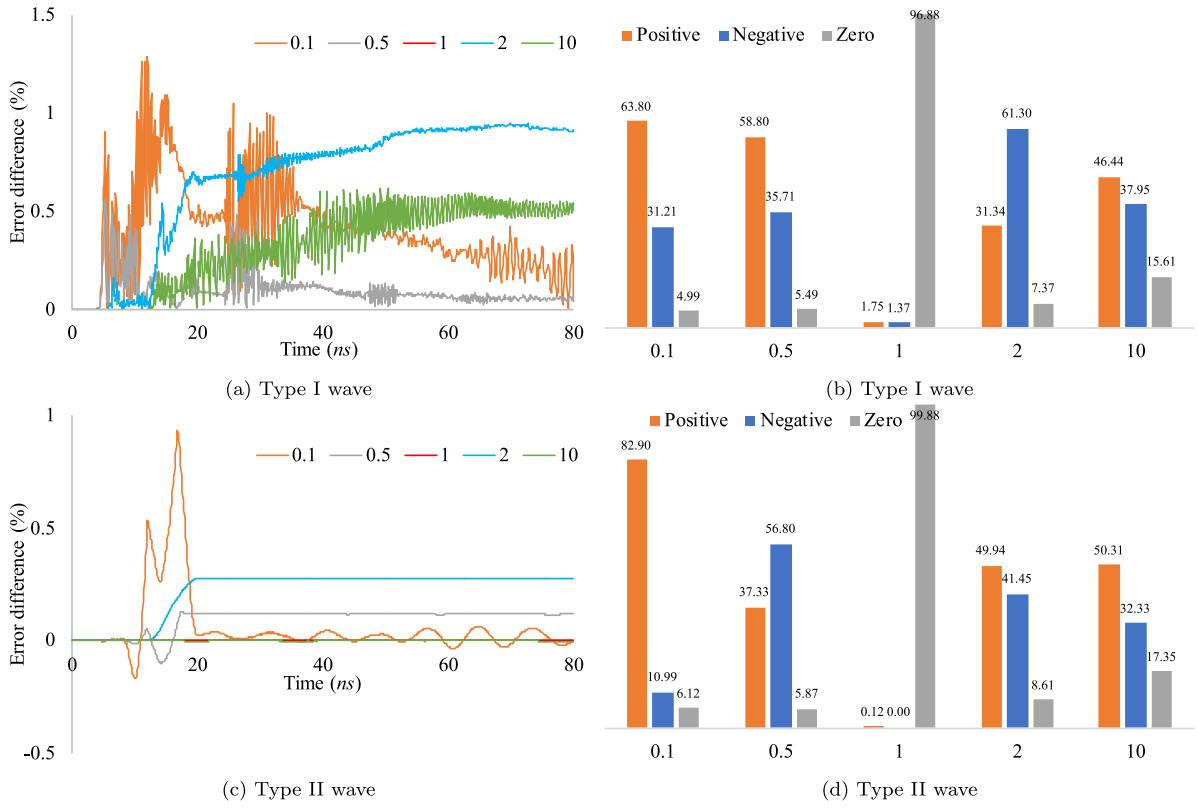


Fig. 10. Error comparison between the proposed homogenization scheme and the linear homogenization scheme for the effective stiffness matrix. For (a) and (c): error difference for the total mechanical energy, for (b) and (d): percentages of the positive/negative error difference for the mechanical energy within the phase/grain α (unit: %).

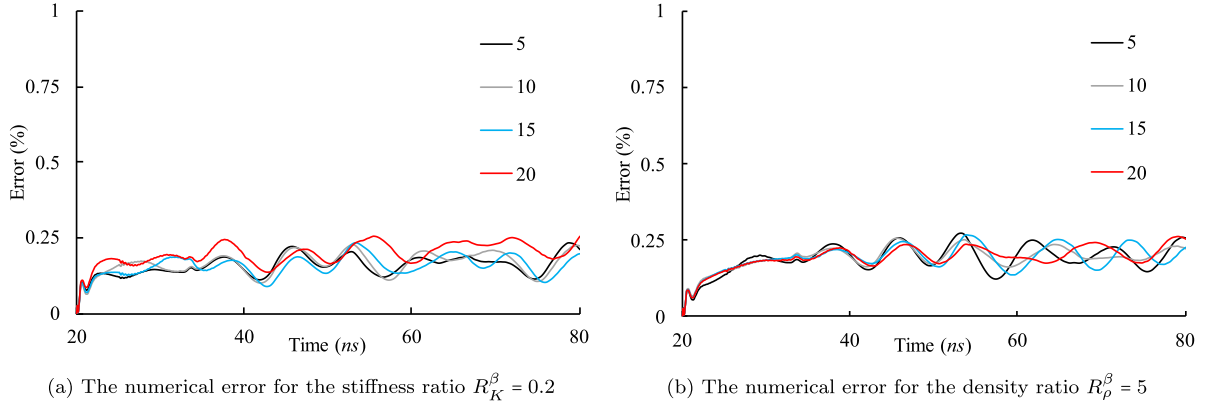


Fig. 11. The numerical error of the total mechanical energy, when the inner phase/grain has different radii and a sharp interface.

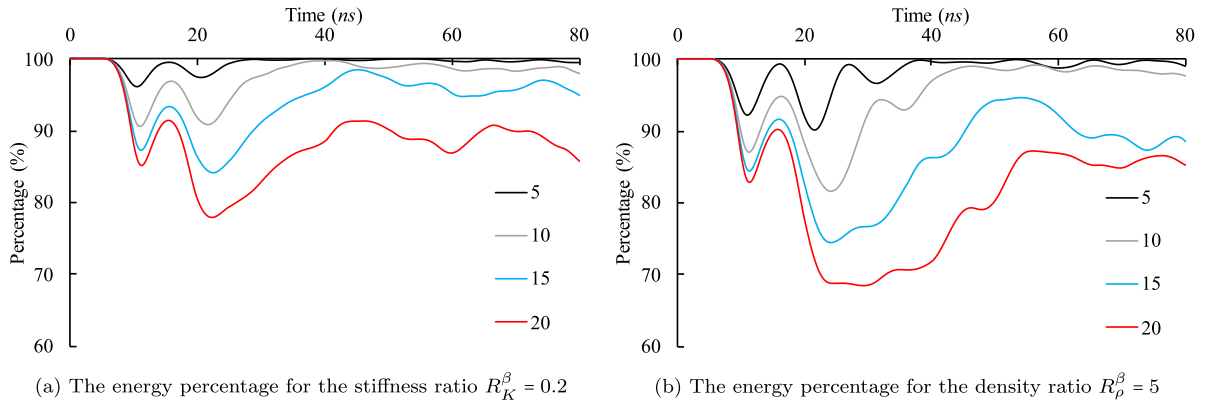


Fig. 12. The percentage of mechanical energy within the phase/grain α , when the inner phase/grain has different radii and a sharp interface.

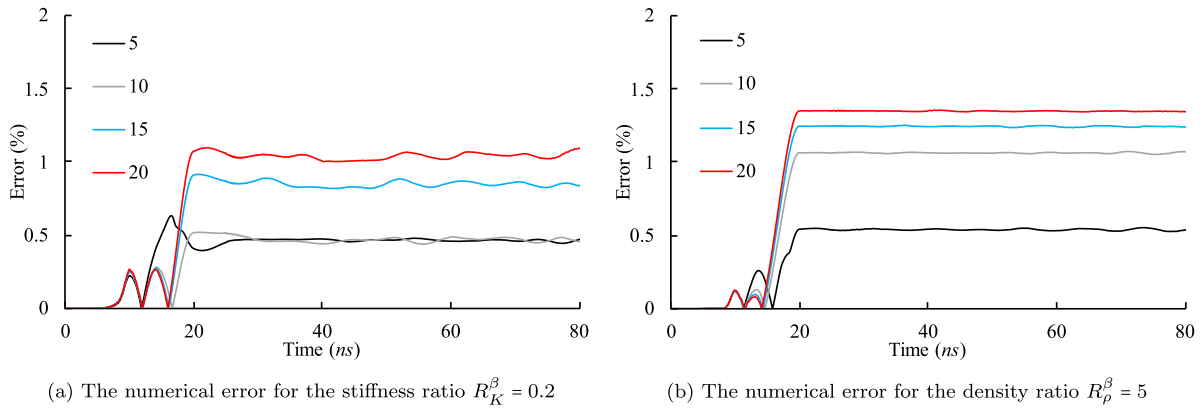


Fig. 13. The numerical error of the total mechanical energy, caused by replacing the sharp interface with a diffuse interface, when the inner phase/grain has different radii.

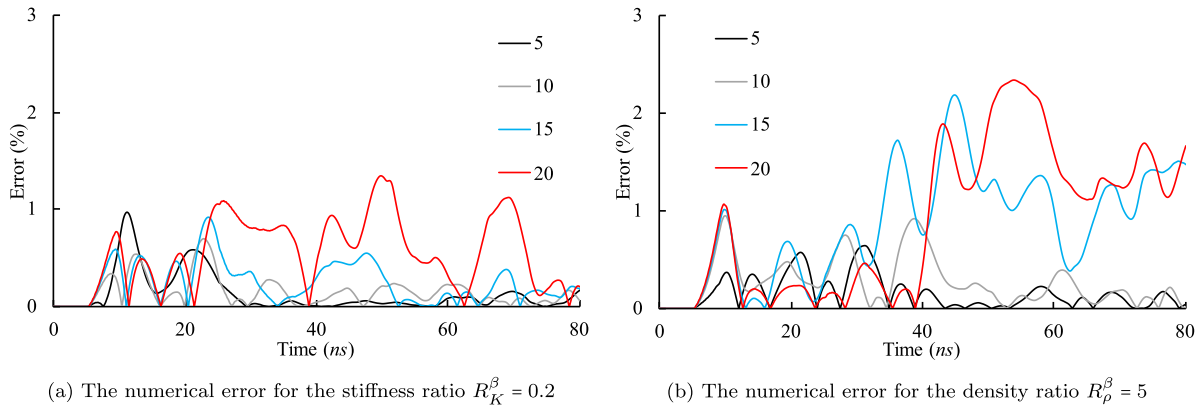


Fig. 14. The numerical error of the energy percentage within the phase/grain α , caused by replacing the sharp interface with a diffuse interface, when the inner phase/grain has different radii.

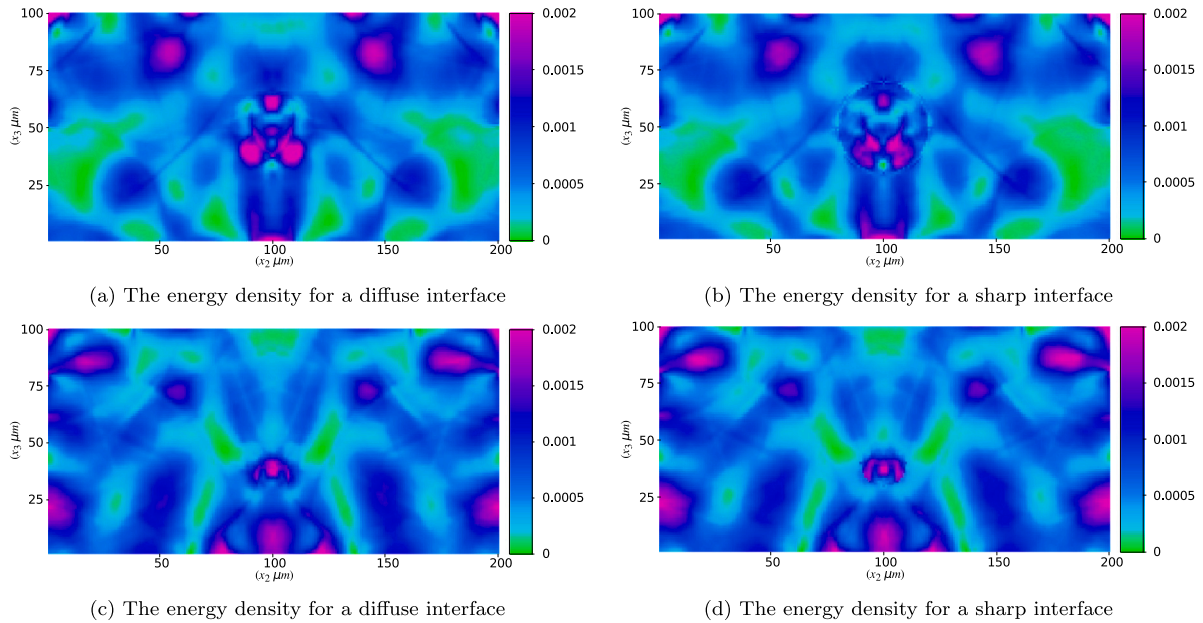


Fig. 15. The mechanical energy density for (a) and (b): the radius of the inner phase/grain is 20 μm , the stiffness ratio $R_K^\beta = 0.2$ and time $t = 70$ ns, for (c) and (d): the radius of the inner phase/grain is 10 μm , the density ratio $R_\rho^\beta = 5$ and time $t = 80$ ns (unit: $10E+04$ J/m³).

For a radius of 20 μm ($R_K^\beta = 0.2$, at $t = 70$ ns) and for a radius of 10 μm ($R_\rho^\beta = 5$, at $t = 80$ ns), the mechanical energy density from the diffuse interface case is compared to the sharp interface case, as

illustrated in Fig. 15. It is observed that the numerical results from these two cases agree well with each other, and that the energy density is smoothly diffused at the interface in Figs. 15(a) and 15(c).

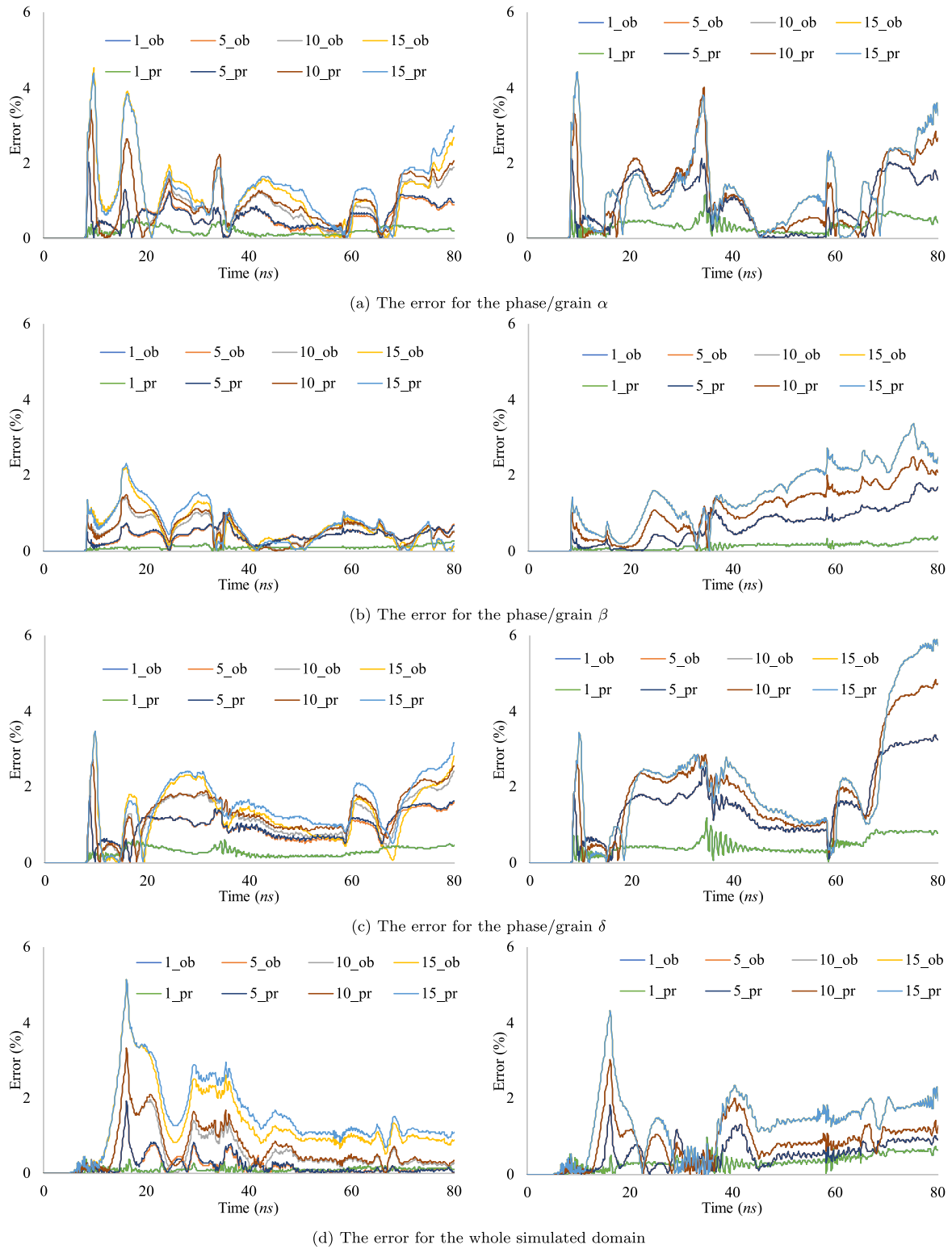


Fig. 16. The error of the mechanical energy for each phase/grain and the whole simulated domain, when loading with the Type I wave (left figures: $R_K^\beta = 0.5$ and $R_K^\delta = 0.1$, right figures: $R_\rho^\beta = 2$ and $R_\rho^\delta = 10$).

7.3. Multiphase/multigrain interface

The numerical example in Fig. 2 is studied as a representative section of a multiphase/multigrain domain. The domain size, the cell size, the origin of the global Cartesian coordinate system and the boundary conditions are the same with Section 7.1, except that the

frequency of the incident wave is 20 MHz. According to the material properties, the simulation can be categorized into two groups, as listed in Table 3. In the first group, $R_K^\beta = 0.5$, $R_K^\delta = 0.1$ and $R_\rho^\beta = R_\rho^\delta = 1$, while $R_\rho^\beta = 2$, $R_\rho^\delta = 10$ and $R_K^\beta = R_K^\delta = 1$ in the second group. For each group, both Types I and II of loading are applied and the wave responses are analysed. The parameter ϵ varies from 1 to 15

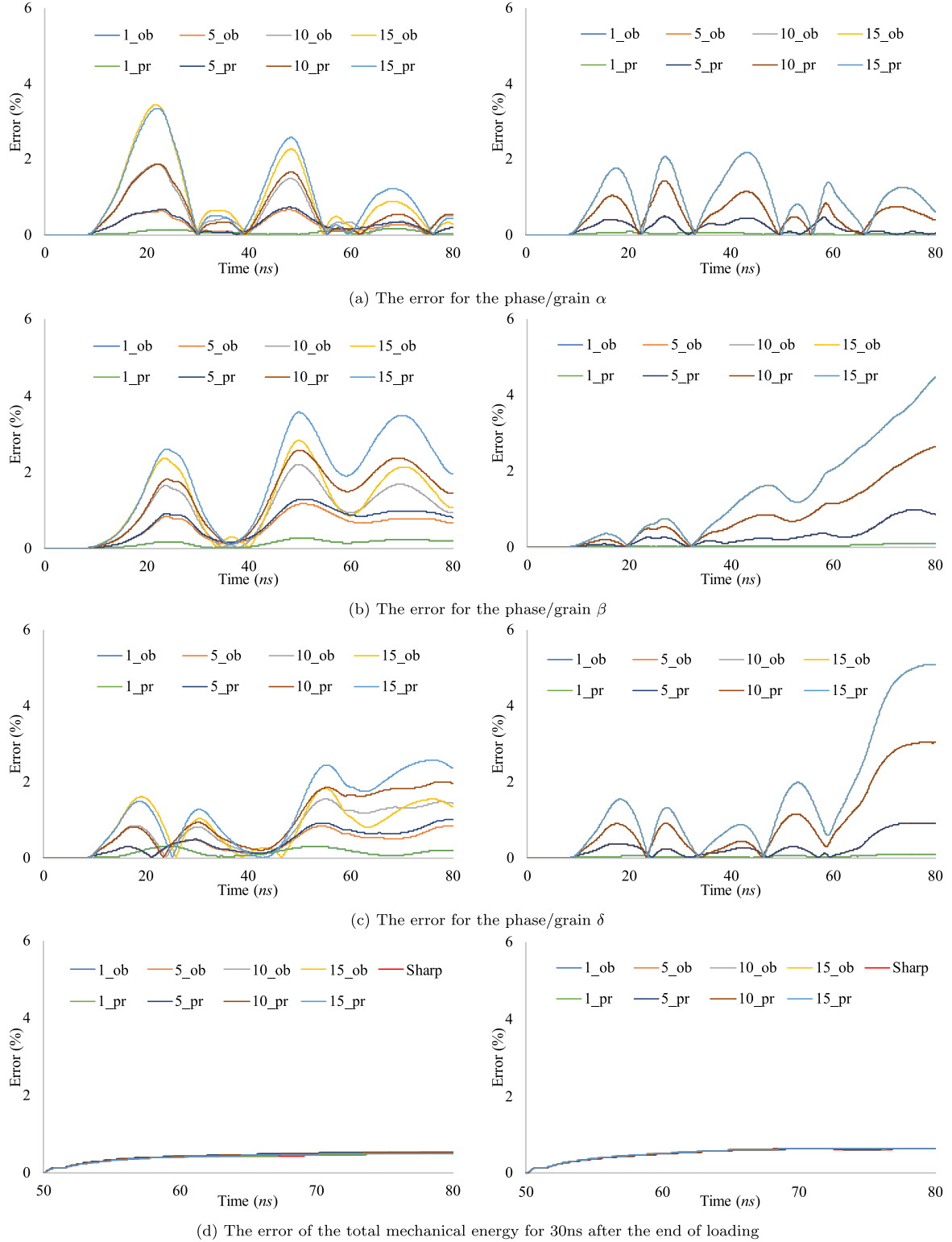


Fig. 17. The error of the mechanical energy for each phase/grain and the whole simulated domain, when loading with the Type II wave (left figures: $R_k^\beta = 0.5$ and $R_k^\delta = 0.1$, right figures: $R_k^\beta = 2$ and $R_k^\delta = 10$).

to determine the influence of the interface width on the numerical results. Here, Eq. (5) applies for the relationship between the interface width and the parameter ϵ . Moreover, the normal vector derived from Eqs. (24a) and (25), i.e. M_{ob} and M_{pr} , is used respectively.

The numerical results from the diffuse interface case are compared with those from the sharp interface case. The errors of the total mechanical energy for each phase/grain and the whole simulated domain are respectively presented in Fig. 16 for Type I and in Fig. 17 for Type

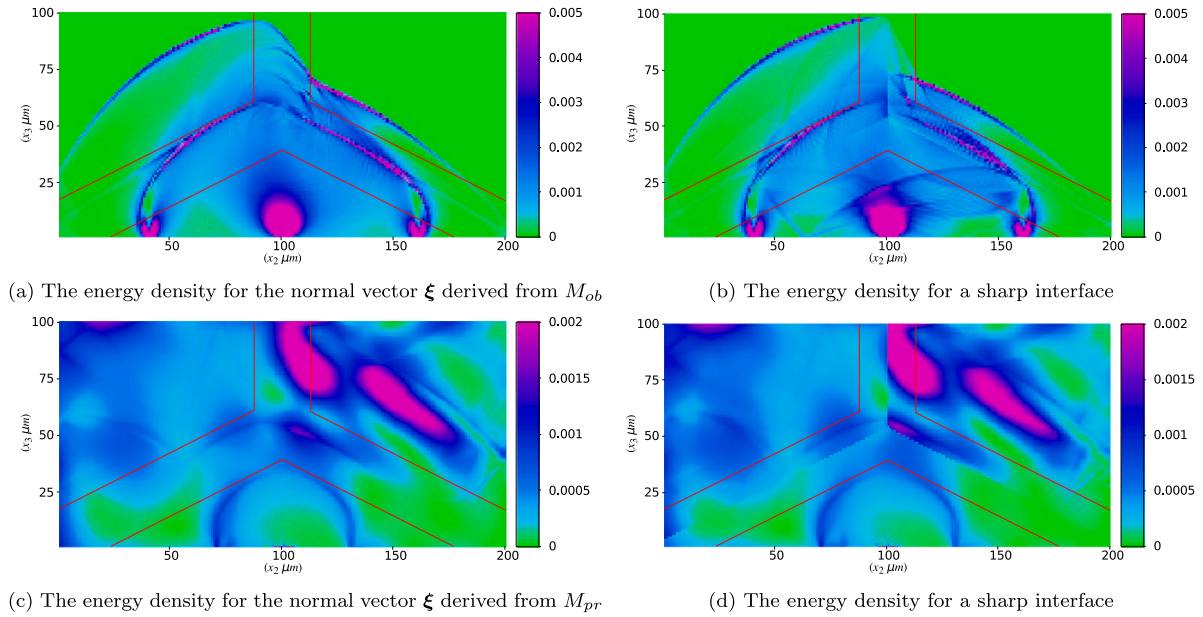


Fig. 18. The mechanical energy density for (a) and (b): $R_K^\beta = 0.5$, $R_K^\delta = 0.1$ and $t = 20$ ns with Type I wave, for (c) and (d): $R_\rho^\beta = 2$, $R_\rho^\delta = 10$ and $t = 60$ ns with Type II wave (unit: $10E + 04$ J/m³).

Table 3
Simulation setup for the numerical example in Fig. 2.

Group	R_K		R_ρ		Wave type	ϵ			M_{ge}	
	β	δ	β	δ						
1	0.5	0.1	1	1	I & II	1	5	10	15	M_{ob} M_{pr}
2	1	1	2	10	I & II	1	5	10	15	M_{ob} M_{pr}

II wave propagation. In Fig. 16(d), the error is calculated by comparing the results from the diffuse interface case with the sharp interface case, while in Fig. 17(d), the total mechanical energy is compared with the value at the end of loading. Generally, the error increases along with the increase of the parameter ϵ , or the interface width. But it is less than 4% for most cases. During the numerical simulation with the phase field method, the parameter ϵ is usually designed as approximately 5. This means that the diffuse interface contains around 13 cells in the normal direction. For almost all cases in Figs. 16 and 17, the corresponding error is less than 2%. For $R_\rho^\beta = 2$ and $R_\rho^\delta = 10$, comparing the numerical results from M_{ob} and M_{pr} , they are almost identical to each other, when the parameter ϵ is fixed. But they are different for $R_K^\beta = 0.5$ and $R_K^\delta = 0.1$, because the effective stiffness is dependent on the normal vector ξ , as derived in Section 3.1. In Eqs. (19) and (22), the matrix Q is also derived based on the normal vector ξ . But the density matrix \widehat{M}^α is a scalar matrix, since the density is isotropic. The transformation in Eqs. (19) and (22) is implemented for an easy understanding of the derivation precondition and procedure (Liu et al., 2021). Therefore, the effective density is independent on the normal vector ξ . In the case of $R_K^\beta = 0.5$ and $R_K^\delta = 0.1$, the numerical error for M_{ob} is generally less than M_{pr} . When increasing the parameter ϵ , the difference becomes greater.

For $\epsilon = 10$, the energy density from the diffuse and sharp interface cases is presented in Figs. 18 and 19. In Figs. 18(a) and 18(c), the area between the parallel red lines is the diffuse interface. For the purpose of comparison, the red lines are also plotted in Figs. 18(b) and 18(d). It is noticed that the energy density is successfully diffused within the two and multi phase/grain interface, and that the energy density within the single phase/grain domain agrees well with the sharp interface case. This can also be observed in Fig. 19. For the normal vector ξ

respectively derived from M_{ob} and M_{pr} , the energy density maps in Fig. 19(b) are almost identical, while they are different in Fig. 19(a), since the effective stiffness is dependent on the normal vector ξ . This coincides with the observation from Figs. 16 and 17. In Fig. 19(a), the energy density is equally weighted by the phases/grains α , β and δ , when the normal vector ξ is derived from M_{ob} , while the phase/grain δ plays a dominant role when ξ is from M_{pr} . This is similar to the difference between Figs. 2(b) and 2(c).

Similar to Section 7.1, with the parameter ϵ ranging from 1 to 15, the homogenization scheme for the effective stiffness matrix in Section 3.1 is compared with the linear homogenization method, i.e. the VT model, through the difference of the numerical errors, as illustrated in Fig. 20. In Fig. 20(a), the positive and negative error differences for the mechanical energy within the phase/grain α are respectively integrated with time t . In Figs. 20(b) and 20(c), the positive/negative error differences for the mechanical energy within the phases/grains β and δ are averaged with the time t . Furthermore, in Fig. 20(d), the error difference for the total mechanical energy is plotted against the time t . The conclusion from Fig. 20 is the same with Section 7.1. Generally, the proposed homogenization scheme performs better than the linear homogenization method.

8. Conclusions

Based on the previous work in Liu et al. (2021), a detailed accuracy and convergence study on the dynamic mechanical energy in two and multi phase/grain systems is implemented in this paper. Factors such as the wave types, the material properties, the phase/grain size, the interface width and the normal vector formula at the multiphase/multigrain interface are considered, and a detailed error discussion is provided.

The numerical results from the diffuse interface case are compared with those from the sharp interface case to verify the numerical accuracy and stability of the proposed scheme. Generally, the numerical errors between these two cases are less than 3%. The numerical solver is robust and stable, which can be applied to a wide range of stiffness/density ratios, phase/grain sizes and interface widths. The numerical results from the Type II wave propagation with weak discontinuity are more accurate and stable than those from the Type I with strong discontinuity, which is consistent with the observation in Liu et al. (2021). The energy conservation law is well recovered, especially

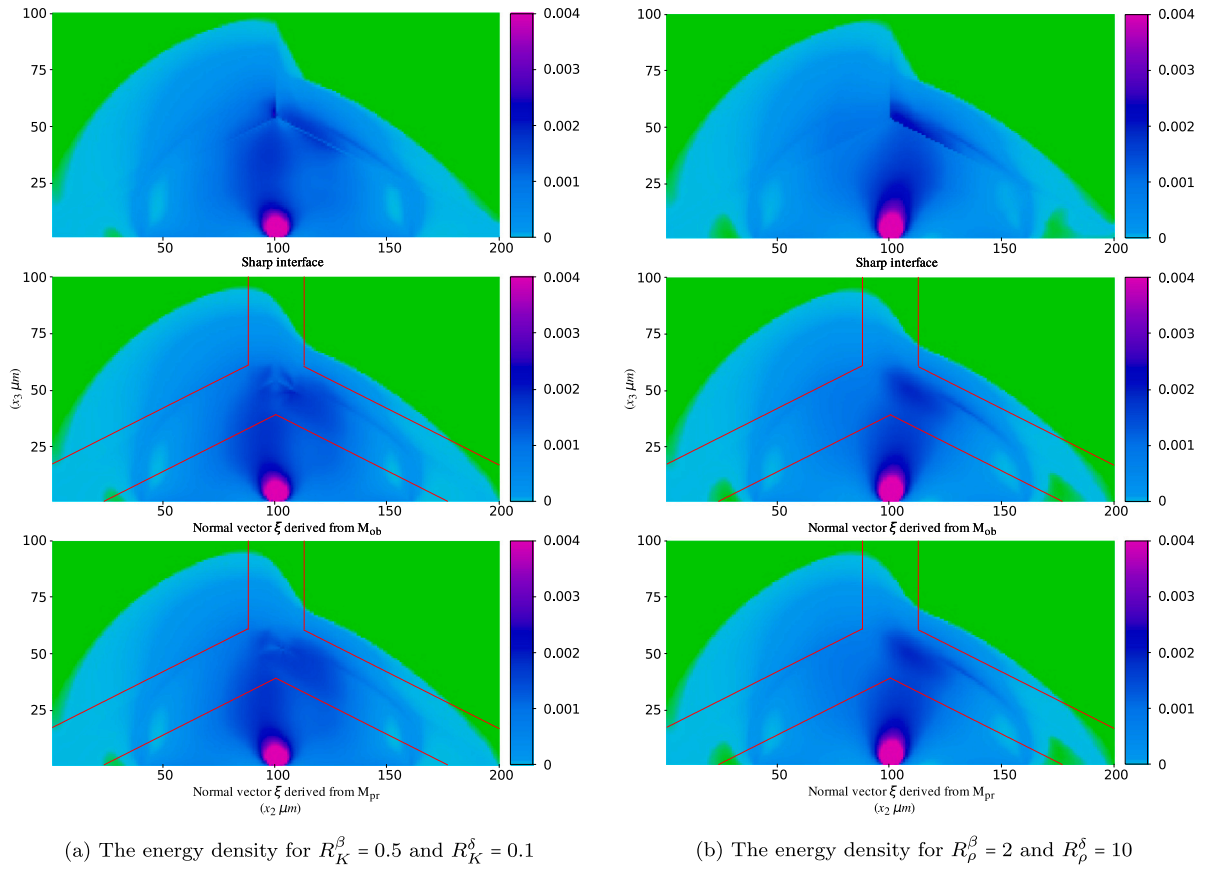


Fig. 19. The mechanical energy density for the Type II wave at $t = 20$ ns (unit: $10E + 04 \text{ J/m}^3$).

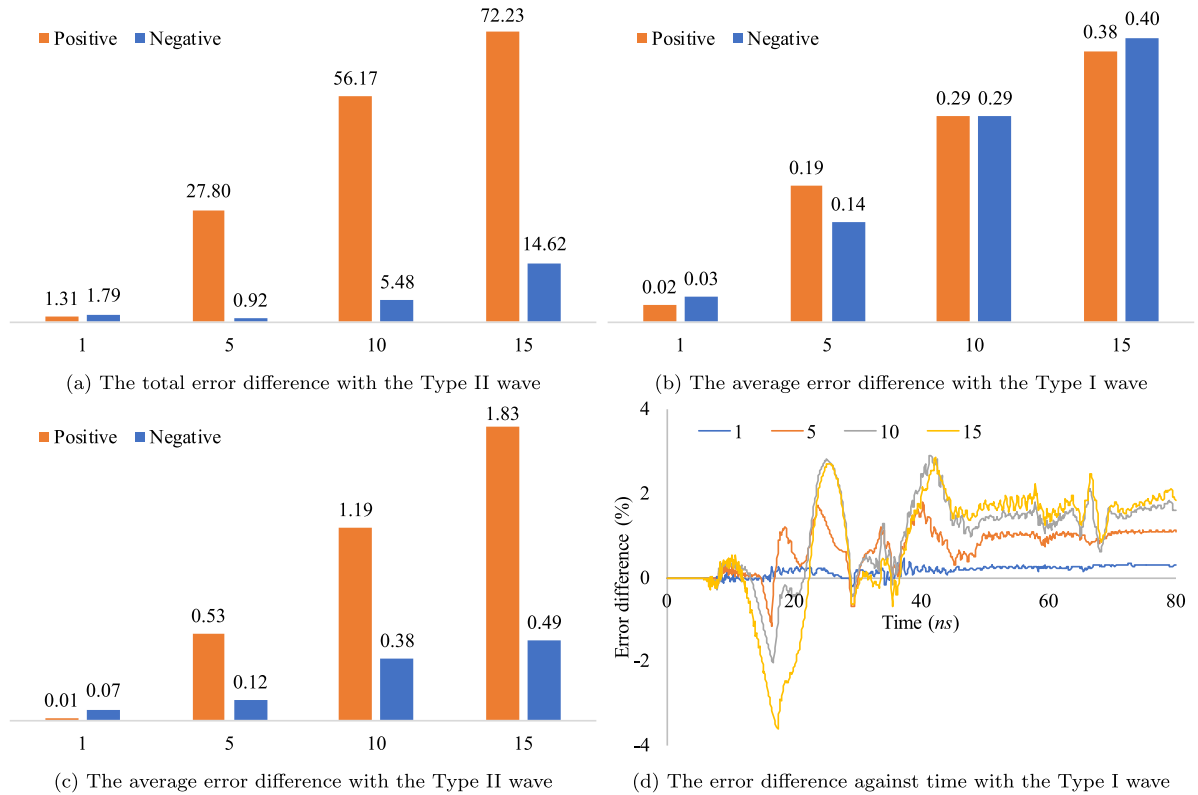


Fig. 20. Error comparison between the proposed homogenization scheme and the linear homogenization scheme for the effective stiffness matrix. (a), (b) and (c) respectively illustrate the error differences for the mechanical energy within the phases/grains α , β and δ for 80 ns with $\Delta t = 0.1$ ns (unit: %), while (d) illustrates the error difference for the total mechanical energy.

$T^{S_\zeta} =$

$$\begin{pmatrix} \xi_1 \xi_1 & \eta_1 \eta_1 & \zeta_1 \zeta_1 & 2\eta_1 \zeta_1 & 2\xi_1 \zeta_1 & 2\xi_1 \eta_1 & 0 & 0 & 0 \\ \xi_2 \xi_2 & \eta_2 \eta_2 & \zeta_2 \zeta_2 & 2\eta_2 \zeta_2 & 2\xi_2 \zeta_2 & 2\xi_2 \eta_2 & 0 & 0 & 0 \\ \xi_3 \xi_3 & \eta_3 \eta_3 & \zeta_3 \zeta_3 & 2\eta_3 \zeta_3 & 2\xi_3 \zeta_3 & 2\xi_3 \eta_3 & 0 & 0 & 0 \\ \xi_2 \xi_3 & \eta_2 \eta_3 & \zeta_2 \zeta_3 & \eta_2 \zeta_3 + \eta_3 \zeta_2 & \xi_2 \zeta_3 + \xi_3 \zeta_2 & \xi_2 \eta_3 + \xi_3 \eta_2 & 0 & 0 & 0 \\ \xi_1 \xi_3 & \eta_1 \eta_3 & \zeta_1 \zeta_3 & \eta_1 \zeta_3 + \eta_3 \zeta_1 & \xi_1 \zeta_3 + \xi_3 \zeta_1 & \xi_1 \eta_3 + \xi_3 \eta_1 & 0 & 0 & 0 \\ \xi_1 \xi_2 & \eta_1 \eta_2 & \zeta_1 \zeta_2 & \eta_1 \zeta_2 + \eta_2 \zeta_1 & \xi_1 \zeta_2 + \xi_2 \zeta_1 & \xi_1 \eta_2 + \xi_2 \eta_1 & 0 & 0 & 0 \\ 0 & 0 & 0 & 0 & 0 & 0 & \xi_1 & \eta_1 & \zeta_1 \\ 0 & 0 & 0 & 0 & 0 & 0 & \xi_2 & \eta_2 & \zeta_2 \\ 0 & 0 & 0 & 0 & 0 & 0 & \xi_3 & \eta_3 & \zeta_3 \end{pmatrix} \quad (\text{A.7})$$

Box I.

for the Type II mechanical load. The energy density is successfully diffused across the interface. In comparison with the effective density, the effective stiffness is more sensitive to the formula of the normal vector. Overall, however, the difference generated by the different normal vector formulas is negligible. Within the multiphase/multigrain interface domain, the influence of the normal vector formulas upon the mechanical energy density can be observed for the case with different stiffness ratios. To be specific, the energy density is equally weighted within the multiphase/multigrain interface domain in Eq. (24a), while the phase/grain with a high stiffness value dominates the energy distribution in Eq. (25). This coincides with the directions of the normal vectors within the multiphase/multigrain interface domain. For the case with different density ratios, however, there is no difference for the energy density within the multiphase/multigrain interface domain. The numerical results are also compared with those from the linear homogenization method, i.e. the VT model. It is observed that the proposed homogenization scheme in Section 3 generally performs better than the linear homogenization method.

Overall, the numerical analysis in this paper builds a solid foundation for the further simulation of mechanical wave associated phase transformation, such as the martensitic transformation Eckner et al. (2016), Kashchenko et al. (2010a,b), Kashchenko (2006).

Furthermore, the established phase field model including the mechanical wave can be applied to computationally quantify phase/grain distributions in composite materials, such as fibre reinforced polymers, or to detect microcracks in a non destructive way in future research.

Declaration of competing interest

The authors declare that they have no known competing financial interests or personal relationships that could have appeared to influence the work reported in this paper.

Data availability

The data that has been used is confidential.

Acknowledgements

This work was financially supported by the China and Germany Postdoctoral Exchange Program 2019 from the Office of China Postdoctoral Council and the Helmholtz Centre (Grant No. : 20191031). Contributions to the modelling formulation were made at CELEST (Center for Electrochemical Energy Storage Ulm Karlsruhe) and partially funded by the German Research Foundation (DFG) under the project ID 390874152 (POLiS Cluster of Excellence). Furthermore we acknowledge the support from Helmholtz association, Germany through the programme ‘‘MSE No.: 43.31.01’’. The authors gratefully acknowledge the editorial support of Leon Geisen and thank all contributors to the PACE3D framework.

Appendix

The transformation matrices M_ϵ , M_σ and Q are composed of the local base unit vectors $\{\xi, \eta, \zeta\}$ as follows:

$$M_\epsilon = \begin{pmatrix} \xi_1 \xi_1 & \xi_2 \xi_2 & \xi_3 \xi_3 & \xi_2 \xi_3 & \xi_1 \xi_3 & \xi_1 \xi_2 \\ 2\xi_1 \zeta_1 & 2\xi_2 \zeta_2 & 2\xi_3 \zeta_3 & \xi_2 \zeta_3 + \xi_3 \zeta_2 & \xi_1 \zeta_3 + \xi_3 \zeta_1 & \xi_1 \zeta_2 + \xi_2 \zeta_1 \\ 2\xi_1 \eta_1 & 2\xi_2 \eta_2 & 2\xi_3 \eta_3 & \xi_2 \eta_3 + \xi_3 \eta_2 & \xi_1 \eta_3 + \xi_3 \eta_1 & \xi_1 \eta_2 + \xi_2 \eta_1 \\ \eta_1 \eta_1 & \eta_2 \eta_2 & \eta_3 \eta_3 & \eta_2 \eta_3 & \eta_1 \eta_3 & \eta_1 \eta_2 \\ \zeta_1 \zeta_1 & \zeta_2 \zeta_2 & \zeta_3 \zeta_3 & \zeta_2 \zeta_3 & \zeta_1 \zeta_3 & \zeta_1 \zeta_2 \\ 2\eta_1 \zeta_1 & 2\eta_2 \zeta_2 & 2\eta_3 \zeta_3 & \eta_2 \zeta_3 + \eta_3 \zeta_2 & \eta_1 \zeta_3 + \eta_3 \zeta_1 & \eta_1 \zeta_2 + \eta_2 \zeta_1 \end{pmatrix} \quad (\text{A.1})$$

$$M_\sigma = \begin{pmatrix} \xi_1 \xi_1 & \xi_2 \xi_2 & \xi_3 \xi_3 & 2\xi_2 \xi_3 & 2\xi_1 \xi_3 & 2\xi_1 \xi_2 \\ \xi_1 \zeta_1 & \xi_2 \zeta_2 & \xi_3 \zeta_3 & \xi_2 \zeta_3 + \xi_3 \zeta_2 & \xi_1 \zeta_3 + \xi_3 \zeta_1 & \xi_1 \zeta_2 + \xi_2 \zeta_1 \\ \xi_1 \eta_1 & \xi_2 \eta_2 & \xi_3 \eta_3 & \xi_2 \eta_3 + \xi_3 \eta_2 & \xi_1 \eta_3 + \xi_3 \eta_1 & \xi_1 \eta_2 + \xi_2 \eta_1 \\ \eta_1 \eta_1 & \eta_2 \eta_2 & \eta_3 \eta_3 & 2\eta_2 \eta_3 & 2\eta_1 \eta_3 & 2\eta_1 \eta_2 \\ \zeta_1 \zeta_1 & \zeta_2 \zeta_2 & \zeta_3 \zeta_3 & 2\xi_2 \xi_3 & 2\xi_1 \xi_3 & 2\xi_1 \xi_2 \\ \eta_1 \zeta_1 & \eta_2 \zeta_2 & \eta_3 \zeta_3 & \eta_2 \zeta_3 + \eta_3 \zeta_2 & \eta_1 \zeta_3 + \eta_3 \zeta_1 & \eta_1 \zeta_2 + \eta_2 \zeta_1 \end{pmatrix} \quad (\text{A.2})$$

$$Q = \begin{pmatrix} \xi_1 & \xi_2 & \xi_3 \\ \eta_1 & \eta_2 & \eta_3 \\ \zeta_1 & \zeta_2 & \zeta_3 \end{pmatrix} \quad (\text{A.3})$$

According to the wave equation and the constitutive equation, the coefficient matrix C^k is expressed as:

$$C^1 = \begin{pmatrix} 0 & 0 & 0 & 0 & 0 & 0 & K_{11} & 0 & 0 \\ 0 & 0 & 0 & 0 & 0 & 0 & K_{21} & 0 & 0 \\ 0 & 0 & 0 & 0 & 0 & 0 & K_{31} & 0 & 0 \\ 0 & 0 & 0 & 0 & 0 & 0 & 0 & 0 & 0 \\ 0 & 0 & 0 & 0 & 0 & 0 & 0 & 0 & K_{55} \\ 0 & 0 & 0 & 0 & 0 & 0 & 0 & K_{66} & 0 \\ \frac{1}{M_{11}} & 0 & 0 & 0 & 0 & 0 & 0 & 0 & 0 \\ 0 & 0 & 0 & 0 & 0 & \frac{1}{M_{22}} & 0 & 0 & 0 \\ 0 & 0 & 0 & 0 & \frac{1}{M_{33}} & 0 & 0 & 0 & 0 \end{pmatrix} \quad (\text{A.4})$$

$$C^2 = \begin{pmatrix} 0 & 0 & 0 & 0 & 0 & 0 & 0 & K_{12} & 0 \\ 0 & 0 & 0 & 0 & 0 & 0 & 0 & K_{22} & 0 \\ 0 & 0 & 0 & 0 & 0 & 0 & 0 & K_{32} & 0 \\ 0 & 0 & 0 & 0 & 0 & 0 & 0 & 0 & K_{44} \\ 0 & 0 & 0 & 0 & 0 & 0 & 0 & 0 & 0 \\ 0 & 0 & 0 & 0 & 0 & 0 & K_{66} & 0 & 0 \\ 0 & 0 & 0 & 0 & 0 & \frac{1}{M_{11}} & 0 & 0 & 0 \\ 0 & \frac{1}{M_{22}} & 0 & 0 & 0 & 0 & 0 & 0 & 0 \\ 0 & 0 & 0 & \frac{1}{M_{33}} & 0 & 0 & 0 & 0 & 0 \end{pmatrix} \quad (\text{A.5})$$

$$\mathbf{XC}^3 = \begin{pmatrix} 0 & 0 & 0 & 0 & 0 & 0 & 0 & 0 & K_{13} \\ 0 & 0 & 0 & 0 & 0 & 0 & 0 & 0 & K_{23} \\ 0 & 0 & 0 & 0 & 0 & 0 & 0 & 0 & K_{33} \\ 0 & 0 & 0 & 0 & 0 & 0 & 0 & K_{44} & 0 \\ 0 & 0 & 0 & 0 & 0 & 0 & K_{55} & 0 & 0 \\ 0 & 0 & 0 & 0 & \frac{0}{1} & 0 & 0 & 0 & 0 \\ 0 & 0 & 0 & \frac{0}{1} & \mathcal{M}_{11} & 0 & 0 & 0 & 0 \\ 0 & 0 & \frac{0}{1} & \mathcal{M}_{22} & 0 & 0 & 0 & 0 & 0 \\ 0 & 0 & \frac{1}{\mathcal{M}_{33}} & 0 & 0 & 0 & 0 & 0 & 0 \end{pmatrix} \quad (\text{A.6})$$

The transformation matrix T^{S_c} is expressed by the local base unit vectors $\{\xi, \eta, \zeta\}$ as Eq. (A.7) given in Box I.

References

- Allen, S.M., Cahn, J.W., 1972. Ground state structures in ordered binary alloys with second neighbor interactions. *Acta Metall.* 20 (3), 423–433.
- Ambati, M., Gerasimov, T., De Lorenzis, L., 2015. Phase-field modeling of ductile fracture. *Comput. Mech.* 55 (5), 1017–1040.
- Ammar, K., Appolaire, B., Cailletaud, G., Forest, S., 2009. Combining phase field approach and homogenization methods for modelling phase transformation in elastoplastic media. *Eur. J. Comput. Mech./Revue Européenne de Mécanique Numérique* 18 (5–6), 485–523.
- Amos, P.K., Schoof, E., Schneider, D., Nestler, B., 2018. Chemo-elastic phase-field simulation of the cooperative growth of mutually-accommodating widmanstätten plates. *J. Alloys Compd.* 767, 1141–1154.
- Artemev, A., Wang, Y., Khachaturyan, A., 2000. Three-dimensional phase field model and simulation of martensitic transformation in multilayer systems under applied stresses. *Acta Mater.* 48 (10), 2503–2518.
- Cahn, J.W., Hilliard, J.E., 1958. Free energy of a nonuniform system. I. Interfacial free energy. *J. Chem. Phys.* 28 (2), 258–267.
- Chen, Q., Ma, N., Wu, K., Wang, Y., 2004. Quantitative phase field modeling of diffusion-controlled precipitate growth and dissolution in Ti–Al–V. *Scr. Mater.* 50 (4), 471–476.
- Durga, A., Wollants, P., Moelans, N., 2013. Evaluation of interfacial excess contributions in different phase-field models for elastically inhomogeneous systems. *Modelling Simulation Mater. Sci. Eng.* 21 (5), 055018.
- Eckner, R., Krüger, L., Ullrich, C., Rafaja, D., Schlothauer, T., Heide, G., 2016. Microstructure and mechanical properties after shock wave loading of cast CrMnNi TRIP steel. *Metall. Mater. Trans. A* 47 (10), 4922–4932.
- Fantoni, F., Bacigalupo, A., 2020. Wave propagation modeling in periodic elasto-thermo-diffusive materials via multifield asymptotic homogenization. *Int. J. Solids Struct.* 196, 99–128.
- Fantoni, F., Bacigalupo, A., Paggi, M., Reinoso, J., 2020. A phase field approach for damage propagation in periodic microstructured materials. *Int. J. Fract.* 223 (1), 53–76.
- Folch, R., Plapp, M., 2005. Quantitative phase-field modeling of two-phase growth. *Phys. Rev. E* 72 (1), 011602.
- Ginzburg, V.L., Landau, L.D., 1950. On the theory of superconductivity. *Zh. Eksp. Teor. Fiz.* 20, 1064.
- Henry, H., 2019. Limitations of the modelling of crack propagating through heterogeneous material using a phase field approach. *Theor. Appl. Fract. Mech.* 104, 102384.
- Herrmann, C., Schoof, E., Schneider, D., Schwab, F., Reiter, A., Selzer, M., Nestler, B., 2018. Multiphase-field model of small strain elasto-plasticity according to the mechanical jump conditions. *Comput. Mech.* 62 (6), 1399–1412.
- Hötzer, J., Reiter, A., Hierl, H., Steinmetz, P., Selzer, M., Nestler, B., 2018. The parallel multi-physics phase-field framework Pace3D. *J. Comput. Sci.* 26, 1–12.
- Hu, F.Q., Hussaini, M., Rasetarinera, P., 1999. An analysis of the discontinuous Galerkin method for wave propagation problems. *J. Comput. Phys.* 151 (2), 921–946.
- Jacqmin, D., 1999. Calculation of two-phase Navier–Stokes flows using phase-field modeling. *J. Comput. Phys.* 155 (1), 96–127.
- Karma, A., Rappel, W.-J., 1998. Quantitative phase-field modeling of dendritic growth in two and three dimensions. *Phys. Rev. E* 57 (4), 4323.
- Käser, M., Dumbser, M., 2006. An arbitrary high-order discontinuous Galerkin method for elastic waves on unstructured meshes—I. The two-dimensional isotropic case with external source terms. *Geophys. J. Int.* 166 (2), 855–877.
- Kashchenko, M., 2006. The wave model of martensite growth for the FCC-BCC transformation of iron-based alloys. *arXiv preprint Cond-Mat/0601569*.
- Kashchenko, M., Chashchina, V., Vikharev, S., 2010a. Dynamic model of the formation of twinned martensite crystals: I. Control wave process and the removal of degeneracy in twin-boundary orientation. *Phys. Met. Metallogr.* 110 (3), 200–209.
- Kashchenko, M., Chashchina, V., Vikharev, S., 2010b. Dynamic model of the formation of twinned martensite crystals: II. Pretransition states and relationships between the volumes of the twin components. *Phys. Met. Metallogr.* 110 (4), 305–317.
- Khachaturian, A., 1983. *Theory of Structural Transformations in Solids*. John Wiley and Sons, New York, NY.
- Kiefer, B., Furlan, T., Mosler, J., 2017. A numerical convergence study regarding homogenization assumptions in phase field modeling. *Internat. J. Numer. Methods Engrg.* 112 (9), 1097–1128.
- Kronbichler, M., Schoeder, S., Müller, C., Wall, W.A., 2016. Comparison of implicit and explicit hybridizable discontinuous Galerkin methods for the acoustic wave equation. *Internat. J. Numer. Methods Engrg.* 106 (9), 712–739.
- LeVeque, R.J., et al., 2002. *Finite Volume Methods for Hyperbolic Problems*. Vol. 31, Cambridge University Press.
- Li, Y., Hu, S., Henager Jr., C.H., 2019. Microstructure-based model of nonlinear ultrasonic response in materials with distributed defects. *J. Appl. Phys.* 125 (14), 145108.
- Liu, X., Schneider, D., Daubner, S., Nestler, B., 2021. Simulating mechanical wave propagation within the framework of phase-field modelling. *Comput. Methods Appl. Mech. Engrg.* 381, 113842.
- Mamivand, M., Zaeem, M.A., El Kadiri, H., 2013. A review on phase field modeling of martensitic phase transformation. *Comput. Mater. Sci.* 77, 304–311.
- Militzer, M., 2011. Phase field modeling of microstructure evolution in steels. *Curr. Opin. Solid State Mater. Sci.* 15 (3), 106–115.
- Moelans, N., Blanpain, B., Wollants, P., 2008. An introduction to phase-field modeling of microstructure evolution. *CALPHAD* 32 (2), 268–294.
- Mosler, J., Shchyglo, O., Hojjat, H.M., 2014. A novel homogenization method for phase field approaches based on partial rank-one relaxation. *J. Mech. Phys. Solids* 68, 251–266.
- Nakahata, K., Sugahara, H., Barth, M., Köhler, B., Schubert, F., 2016. Three dimensional image-based simulation of ultrasonic wave propagation in polycrystalline metal using phase-field modeling. *Ultrasonics* 67, 18–29.
- Nestler, B., Garcke, H., Stinner, B., 2005. Multicomponent alloy solidification: phase-field modeling and simulations. *Phys. Rev. E* 71 (4), 041609.
- Nestler, B., Wheeler, A.A., 2002. Phase-field modeling of multi-phase solidification. *Comput. Phys. Comm.* 147 (1–2), 230–233.
- Reuß, A., 1929. Berechnung der fließgrenze von mischkristallen auf grund der plastizitätsbedingung für einkristalle. *ZAMM Z. Angew. Math. Mech.* 9 (1), 49–58.
- Schneider, D., Schoof, E., Tschukin, O., Reiter, A., Herrmann, C., Schwab, F., Selzer, M., Nestler, B., 2018. Small strain multiphase-field model accounting for configurational forces and mechanical jump conditions. *Comput. Mech.* 61 (3), 277–295.
- Schneider, D., Schwab, F., Schoof, E., Reiter, A., Herrmann, C., Selzer, M., Böhlke, T., Nestler, B., 2017. On the stress calculation within phase-field approaches: a model for finite deformations. *Comput. Mech.* 60 (2), 203–217.
- Schneider, D., Tschukin, O., Choudhury, A., Selzer, M., Böhlke, T., Nestler, B., 2015. Phase-field elasticity model based on mechanical jump conditions. *Comput. Mech.* 55 (5), 887–901.
- Selzer, M., Nestler, B., Danilov, D., 2010. Influence of the phase diagram on the diffuse interface thickness and on the microstructure formation in a phase-field model for binary alloy. *Math. Comput. Simulation* 80 (7), 1428–1437.
- Spatschek, R., Hartmann, M., Brener, E., Müller-Krumbhaar, H., Kassner, K., 2006. Phase field modeling of fast crack propagation. *Phys. Rev. Lett.* 96 (1), 015502.
- Steinbach, I., Apel, M., 2006. Multi phase field model for solid state transformation with elastic strain. *Physica D* 217 (2), 153–160.
- Steinbach, I., Pezzolla, F., 1999. A generalized field method for multiphase transformations using interface fields. *Physica D* 134 (4), 385–393.
- Voigt, W., 1889. Über die Beziehung zwischen den beiden Elastizitätskonstanten isotroper Körper. *Ann. Phys.* 274 (12), 573–587.
- Wang, L., 2011. *Foundations of Stress Waves*. Elsevier.
- Wang, Y., Li, J., 2010. Phase field modeling of defects and deformation. *Acta Mater.* 58 (4), 1212–1235.
- Wilcox, L.C., Stadler, G., Burstedde, C., Ghattas, O., 2010. A high-order discontinuous Galerkin method for wave propagation through coupled elastic-acoustic media. *J. Comput. Phys.* 229 (24), 9373–9396.
- Wilson, Z.A., Landis, C.M., 2016. Phase-field modeling of hydraulic fracture. *J. Mech. Phys. Solids* 96, 264–290.
- Xi, S., Su, Y., 2021. A phase field study of the grain-size effect on the thermomechanical behavior of polycrystalline NiTi thin films. *Acta Mech.* 232 (11), 4545–4566.
- Xu, Z., Meakin, P., 2008. Phase-field modeling of solute precipitation and dissolution. *J. Chem. Phys.* 129 (1), 014705.
- Yeddu, H.K., Malik, A., Ågren, J., Amberg, G., Borgenstam, A., 2012. Three-dimensional phase-field modeling of martensitic microstructure evolution in steels. *Acta Mater.* 60 (4), 1538–1547.
- Zhang, M.-R., Su, Y., 2022. The negative dielectric permittivity of polycrystalline barium titanate nanofilms under high-strength kHz-AC fields. *Int. J. Solids Struct.* 254, 111939.